Contents

List of Figures

List of Tables

Chapter 1

Enhanced LIGO squeezing experiment

Enhanced LIGO is the most sensitive gravitational wave detector that has been constructed to date. This makes it the best possible test bed for technologies to be used in Advanced detectors. Although Xiao and colleagues first demonstrated an improvement in the sensitivity of an interferometer 25 years ago, [76], practical implementation of squeezing in a full scale gravitational wave detector has only recently become feasible. In the last decade as full scale gravitational wave detectors like LIGO and VIRGO have reached their design sensitivities, research on squeezing has brought the technology closer to begin feasible for gravitational wave detectors. Table top experiments have shown noise reduction in interferometer configurations more similar to gravitational wave detectors, at measurement frequencies of 5 MHz and above [48, 73]. The most promising astrophysics targets for earth based gravitational wave detectors are expected to emit at frequencies from 10s of Hz to a few kHz. A variety of classical noise couplings had to be overcome to produce squeezing at these low frequencies [47,67]. Squeezing down to 30kHz was demonstrated in a prototype LIGO interferometer with 40 meter arms in 2007, [37] and another important step towards implementation in full scale detectors was achieved in 2011 with implementation of squeezing down to 1kHz in the GEO600 detector [15]. The only way to demonstrate squeezing in the LIGO band is to implement squeezing in a LIGO interferometer, and we were fortunate enough to have that opportunity after the end of LIGO's S6 science run. One of the Enhanced LIGO in-

terferometers (H1) was preserved while construction of Advanced LIGO was underway on the other two LIGO interferometers, and a short window of opportunity came in late 2011 when we were able to use the full interferometer. This work is complimentary to the work with squeezing done at GEO600 in the last few years. GEO has been able to implement squeezing as part of normal operation, and study the stability of the level of squeezing and glitches introduced to the interferometer by squeezing. While we had a shorter window of opportunity to test squeezing before construction of Advanced LIGO began, the LIGO interferometers have orders of magnitude better sensitivity in the crucial region around 100Hz. This allowed us to test squeezing in a regime that is the most similar to Advanced LIGO currently available, and understand some of the challenges unique to low frequency squeezing in a very sensitive interferometer, including acoustic noise couplings. We were able to use squeezing to achieve the best sensitivity above 250 Hz that has been demonstrated in a gravitational wave detector to date.

1.1 Enhanced LIGO

The LIGO interferometers have added complexity compared to the simple Michelson discussed in the introduction, which is needed to sense the incredibly small strains produced by gravitational waves. A simplified diagram of the Enhanced LIGO layout is shown in Figure 1-1. The light source is a Nd:YAG laser, capable of producing 35W of 1064nm light. The main laser is prestabilized in frequency and intensity, and filtered by a input mode cleaner to achieve a spatially pure beam for injection into the interferometer.

The core interferometer optics are all suspended from vibration isolated platforms, to reduce the coupling of seismic noise to motion of the optics. An active control system maintains the alignment of these suspended optics, which move relative to the ground [17]. The Michelson interferometer is operated near a dark fringe, so that most of the light incident from the input port of the interferometer is reflected back towards the laser, and only a small fraction is sent toward the antisymmetric port. Because the expected gravitational wave strains are of the order 10^{-21}, the longest practical arm length is needed to increase the

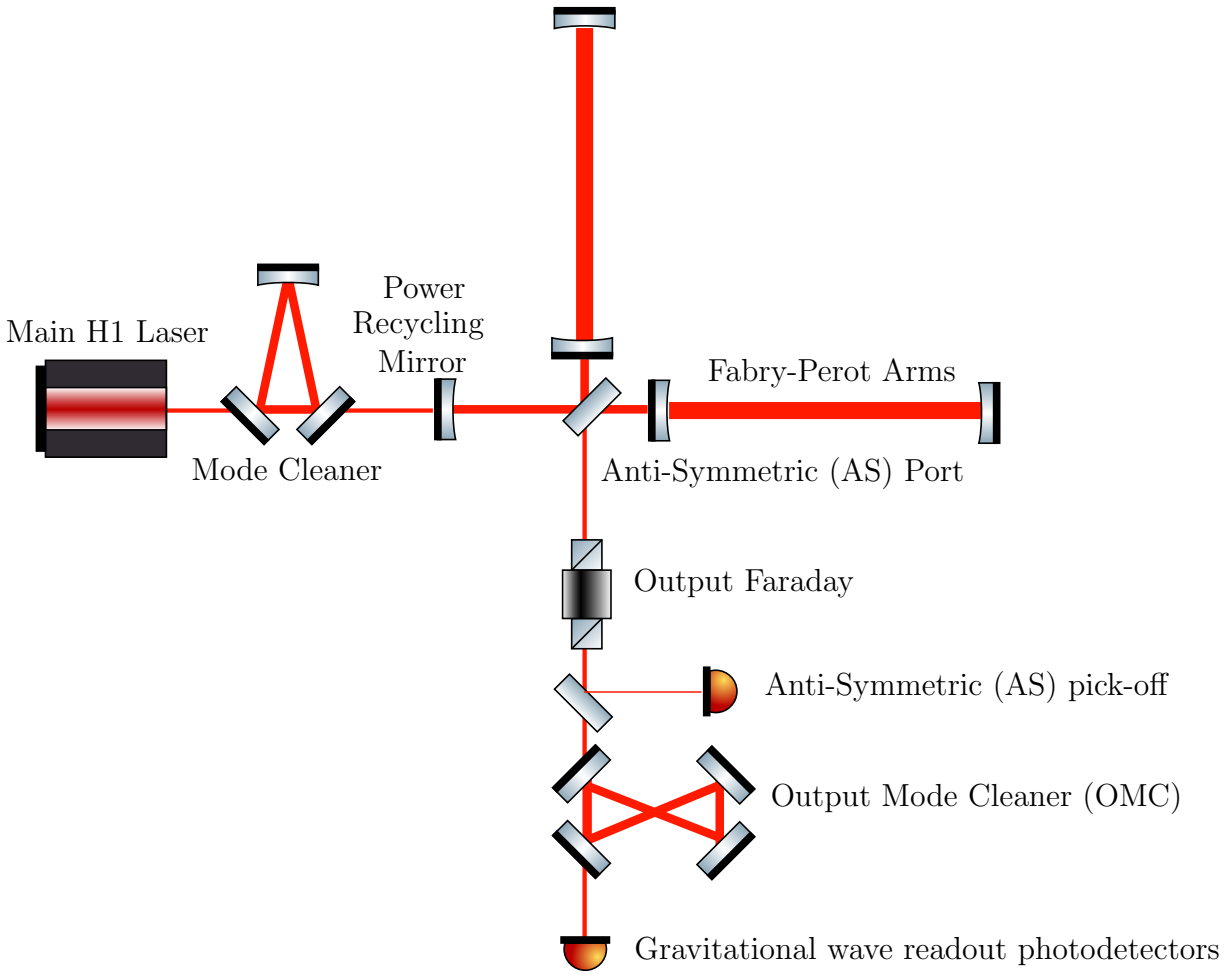

Figure 1-1: Basic layout of Enhanced LIGO, not to scale

expected displacements. The LIGO interferometers use 4km arms, each of which is a Fabry-Perot cavity. The Fabry-Perot circulates light an for an average 130 round trips in each arm before leaking out toward the beam-splitter. This means that the phase shift induced by a low frequency gravitational wave will be enhanced by a factor of about 130. The cavities also act as a low pass filter for the gravitational wave signal, with a cavity pole at 100Hz. The transfer functions of a Fabry-Perot cavity are derived in Appendix **??**. The four optics that make up the Fabry-Perot arms are the test masses used to detect gravitational waves, the mirrors closest to the beam-splitter are called input test masses while the high reflectors at the end of the cavities are known as end test masses.

In addition to the arm cavities, LIGO makes use of a power recycling cavity, a nested cavity formed by the power recycling mirror and the two arm cavities to increase the laser power at the beam-splitter, and further improve the shot noise limited sensitivity. The power recycling cavity increases the power at the beamsplitter by a factor of 40, so that with 20W injected into the interferometer there are 800W at the beamsplitter and 5kW in each arm. The laser power was increased from Intial LIGO to Enhanced LIGO, to improve the shot noise limited sensitivity. This high power presents several practical challenges, [17], including thermal lensing in the input test masses that must be compensated. Advanced LIGO will further increase the power, approaching the limits of available technology. Squeezing provides an alternative to high power operation that will provide an easier and less risky route to better sensitivity at some point, possibly early in the Advanced LIGO era.

The gravitational wave signal is detected using homodyne detection at the antisymmetric port. The low power (100s of mWs) beam leaving the AS port first passes through an output Faraday, to prevent scatter from any of the sensors or optics in the readout chain from reentering the interferometer and creating a parasitic interferometer. The possibility that the squeezer would introduce a parasitic interferometer and add noise to the readout is explored in Chapter **??**. For this experiment, the output Faraday isolator used in initial and enhanced LIGO was replaced with one of the output Faradays that will be used in Advanced LIGO, which allows access to the port used for squeezing injection.

After the output Faraday a small amount of the power at the antisymmetric port is picked off and sent to an out of vacuum table, known as the AS table, with several sensors used for alignment sensing and control, and the heterodyne sensing scheme that is used initially to lock the interferometer. This sensing scheme uses RF modulation sidebands for a locking scheme similar to Pound-Drever-Hall, and at the AS port approximately 2/3 of the optical power was actually from the sidebands at 24.5MHz. For the squeezing experiment the power in this pick off beam was reduced to 1% of the power in the AS beam, to reduce the optical loss in the detection path. To readout the gravitational wave signal enhanced LIGO used an unbalanced homodyne readout, which requires a local oscillator with minimum noise. The

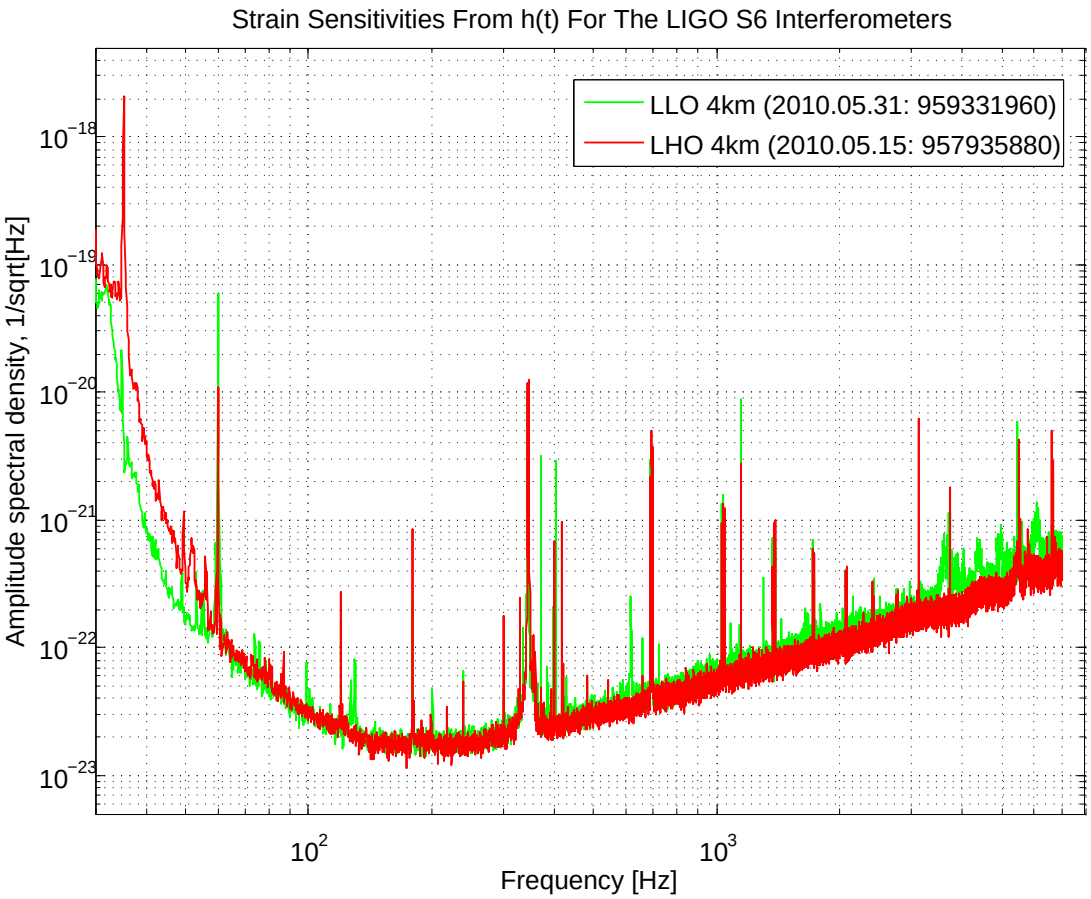

Figure 1-2: Strain sensitivity of enhanced LIGO during S6 science run. (LSC P+P committee)

output mode cleaner filters the AS beam, rejecting the RF sidebands and light in the wrong spatial mode to create a quiet local oscillator [30, 32, 65]. The output mode cleaner(OMC) in the H1 interferometer suffered extra losses in the last part of the Enhanced LIGO science run, which had only a small impact on the sensitivity to gravitational waves, but introduced a 50% loss to the squeezing detection path at the beginning of the squeezing experiment. To reduce the losses, the output mode cleaner from the H1 interferometer was replaced with the Livingston OMC in October 2011. The main results from our experiment were obtained with the Enhanced LIGO interferometer in this configuration, as close as possible to the configuration used during LIGO's flagship S6 science run.

Figure 1-2 shows the strain sensitivity of both the Hanford (H1) and Livingston (L1) Enhanced LIGO detectors. The limiting noise source below 40Hz is seismic noise. Thermal noise from the mirror suspensions and the optical coating dominates from 40Hz-100Hz, and shot noise dominates above 100Hz. Quantum radiation pressure noise is buried orders of magnitudes below the seismic noise in enhanced LIGO, so no quantum radiation pressure effects were accessible during this experiment.

1.2 Squeezed state source

Figure 1-3 shows a simplified layout of the squeezer table. Our two lasers are Nd:YAG non-planar ring oscillators (NPROs). Two frequency stabilization servos (FSS1 and FSS2) keep the pump laser locked to the H1 main laser frequency and the control laser locked at a 29.5MHz offset. The main laser is used to pump a second harmonic generator. This is a standing wave cavity with a periodically poled $KTiOPO_4$ (PPKTP) nonlinear crystal that frequency doubles the infrared light to create the 532nm second harmonic. The length of the SHG is locked to the main laser frequency using a Pound-Drever-Hall (PDH) error signal sensed in transmission, and a piezoelectric transducer (PZT) on one of the cavity mirrors as an actuator. The 532 nm beam produced by the SHG is then used to pump the traveling wave OPO, which also contains a PPKTP crystal. The OPO length is locked to the main laser frequency by a PDH signal sensed in reflection off the cavity. The squeezed beam produced by the OPO is separated from the reflected green beam by a dichroic and sent either to a diagnostic balanced homodyne detector or into the interferometer. The homodyne detector was designed and built at the Max Planck Institute for Gravitational Physics in Hannover Germany. The control laser is injected into a rear coupler on the OPO. Inside the OPO a second symmetric sideband is generated by the nonlinear interaction, these two sidebands are sensed both in reflection off of the OPO rear coupler and at the homodyne detector or the antisymmetric port if squeezing is injected into the interferometer. The combination of the two error signals are used to control the squeezing angle, as will be discussed in chapter ??.

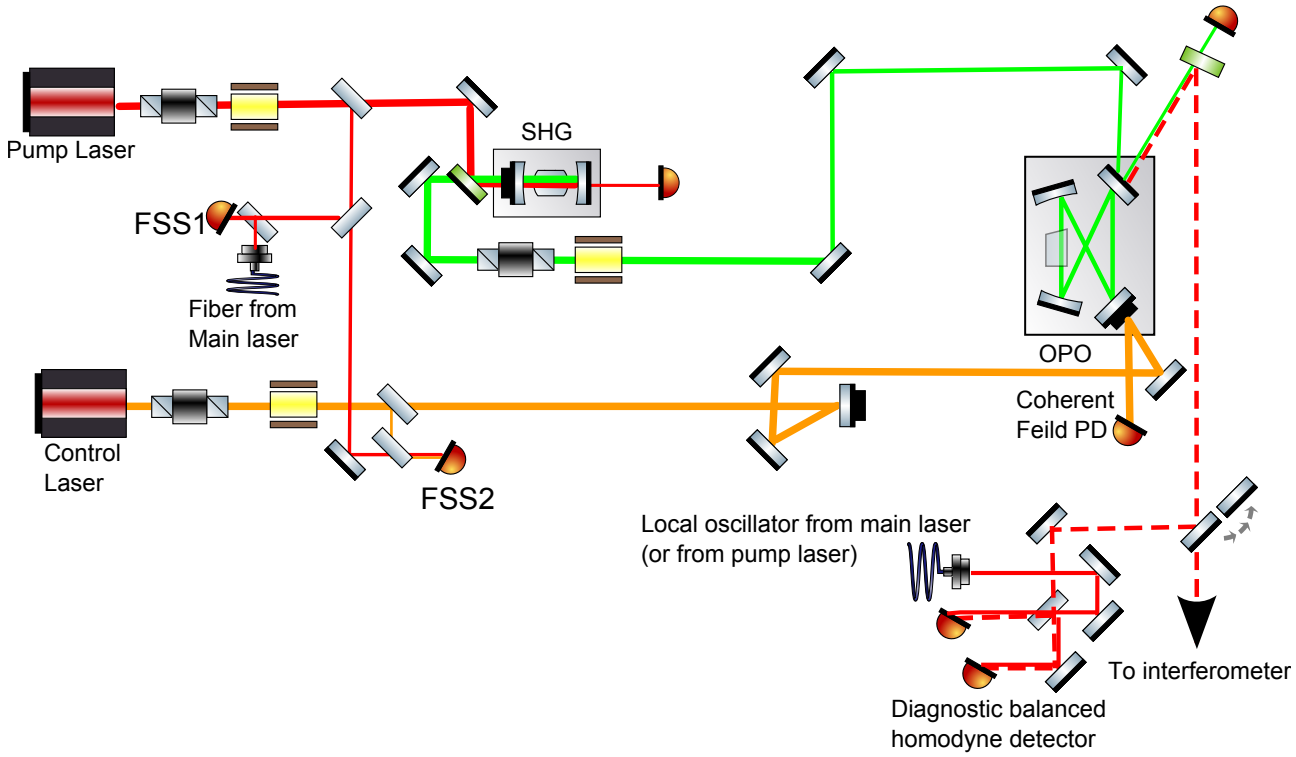

Figure 1-3: Simplified layout of squeezed state source. The pump laser is phase locked to a small amount of light from the main H1 laser. The pump laser is used to pump the second harmonic generator (SHG) which in turn pumps an OPO. A second laser, called the control laser, is offset locked to the pump laser and injected into the OPO through a rear coupler. This field is sensed both in reflection off of the OPO rear coupler and either at the homodyne detector or at the interferometer AS table. The combination of the two error signals are used to control the squeezing angle.

1.2.1 Second harmonic generation in a cavity

Our SHG cavity is based on a design from AEI in Hannover Germany, similar to the SHG described in [11,72]. It uses a very compact design for mechanical and temperature stability.

The SHG process is described by the same cavity equations of motion as we used for the OPO, **??**, **??**, and **??**, now with no incident field in the green but an incident infrared field A^{in}. Since we are not interested in the quantum fluctuations we will drop the vacuum fluctuations $\delta v^{l,inc}$. We also do not need to use the two photon formalism, so the equations become [7,38]:

$$\dot{a}(t) = -(\gamma_{r,shg}^{tot} - i\Delta_a(t))a(t) + \epsilon a^{\dagger}(t)b(t) + \sqrt{2\gamma_{r,shg}^{in}}A^{in} \tag{1.1}$$

$$\dot{b}(t) = -(\gamma_{g,shg}^{tot} - i\Delta_b(t))b(t) - \frac{\epsilon a^2(t)}{2} \tag{1.2}$$

Our SHG is resonant only for the infrared field, with an input coupler anti-reflection coated for green so $\gamma_b^{tot} = \gamma_b^{in} = 1/\tau_{shg}$. Since we are interested in the steady state power produced by the SHG, we set the time derivatives to zero and take the time independent part of these equations [38, p 84]:

$$0 = -\gamma_{r,shg}^{tot}\bar{a} + \frac{\epsilon\bar{a}^*\bar{b}}{2} + \sqrt{2\gamma_a^{in}}\bar{A}^{in} \tag{1.3}$$

$$0 = -\frac{1}{\tau_{shg}}\bar{b} - \frac{\epsilon\bar{a}^2}{2} \tag{1.4}$$

Using 1.4 and the input output relations the output green field in terms of the circulating red field is:

$$\bar{b} = \frac{-\epsilon\bar{a}^2\tau_{shg}}{2} \tag{1.5}$$

$$\bar{B}_{shg}^{out} = \sqrt{2/\tau_{shg}}\bar{b} = -\epsilon\bar{a}^2\sqrt{\frac{\tau_{shg}}{2}} \tag{1.6}$$

The equation for the circulating red field in terms of the incident red field is nonlinear:

$$\bar{a} = \frac{\sqrt{(2\gamma_{r,shg}^{in})}\bar{A}_{in}}{\left(\gamma_{r,shg}^{tot} + \frac{\epsilon^2\tau_{shg}|\bar{a}|^2}{2}\right)} \tag{1.7}$$

The term $\epsilon^2|\bar{a}|^2\tau_{shg}/2$ is the rate at which the infrared field is lost to conversion to green field, so we can write an effective cavity decay rate, which is $\gamma_{shg}^{eff} = \gamma_a^{tot} + \epsilon^2|\bar{a}|^2\tau_{shg}/2$. The conversion efficiency of an SHG is the ratio of input power at the fundamental frequency to output second harmonic power:

$$\eta_{SHG} = \frac{P_{532}}{P_{1064}} = \frac{2|\bar{B}_{out}|^2}{|\bar{A}_{in}|^2} = \frac{2\gamma_{r,shg}^{in}\tau_{shg}\epsilon^2|\bar{a}|^2}{\left(\gamma_{r,shg}^{tot} + \frac{\epsilon^2|\bar{a}|^2\tau_{shg}}{2}\right)^2} \tag{1.8}$$

We can use our SHG conversion efficiency, which was around 50%, and make the approximation that $\gamma_a^{in} \approx \gamma_a^{tot}$ to get an estimate for the value of $\alpha_{shg} = \epsilon^2|\bar{a}|^2\tau_{shg}/2\gamma_{r,shg}^{tot}$ for our SHG in the configuration that we used it.

$$\eta_{shg} = \frac{4\alpha_{shg}}{(1+\alpha_{shg})^2} \tag{1.9}$$

This ratio is the ratio of the field that is converted to green in each round trip to the field that is lost through one of the couplers. With the approximation that $\gamma_a^{in} \approx \gamma_a^{tot}$, the ratio α_{shg} becomes the ratio of the intra-cavity loss to the input coupler transmission, which is 1 for a critically coupled cavity, which would have 100% conversion efficiency. Our SHG, and most SHGs with reasonable input powers, have a value of α_{shg} less than 1. We can confirm this by turning up the input power, in most cases the conversion efficiency will increase with increased input power, meaning that α_{shg} is less than one. With our conversion efficiency of 50%, $\alpha_{shg} \approx 0.17$. This means that in our case, $\gamma_{shg}^{eff} = (1+\alpha_{shg})\gamma_r^{tot} \approx 1.2\gamma_{r,shg}^{tot}$. The best SHG conversion efficiency we measured was 60% [68], 50% was a more typical efficiency.

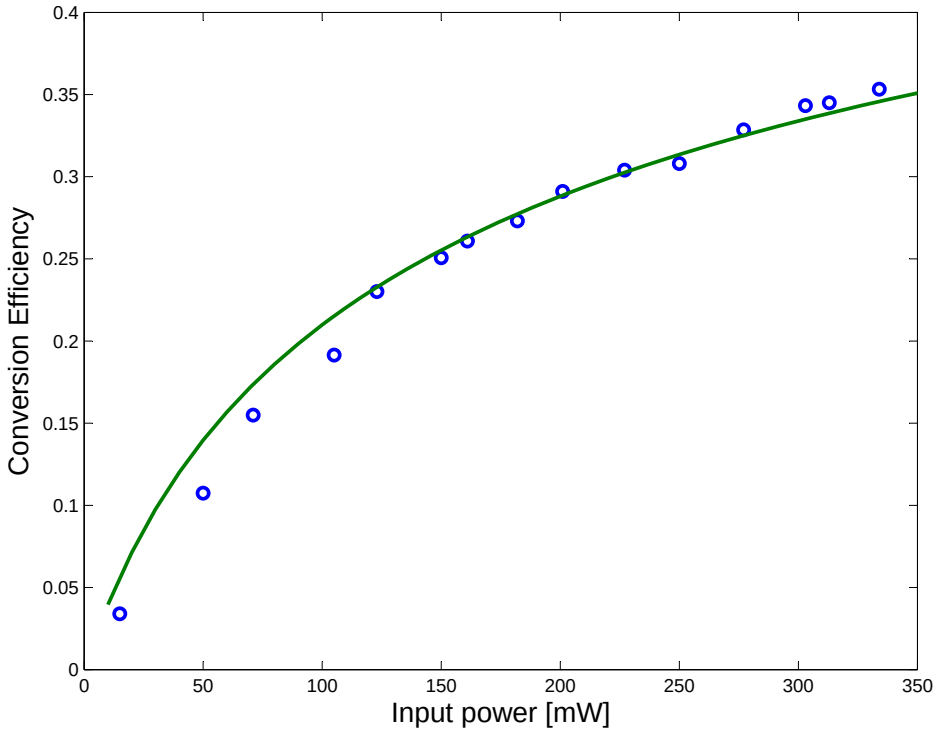

Figure 1-4: Conversion efficiency as a function of input fundamental power [55]. Our measurements are plotted against a numerical solution assuming that the input coupler reflectivity is 90%, the intracavity losses are 2%, and the single pass nonlinear efficiency (harmonic power over fundamental power squared) is 0.17 (1/W)

1.2.2 Phase Matching

For the nonlinear processes in SHG and OPO to be efficient, the phase relationship between the harmonic and fundamental fields needs to stay fixed as the field propagate. If the index of refraction for the infrared and green fields are different, the two fields will acquire different phase shifts as they propagate through the crystal. In the case of SHG, this means that the green field generated would interfere destructively with the propagating green field which was generated earlier, preventing efficient transfer of energy to the green field. The condition for a well phase matched interaction can be formulated as momentum conservation from the

input (annihilated) photons to the output (created) photons:

$$\sum_i \hbar \mathbf{k}_i = \sum_j \hbar \mathbf{k}_j \tag{1.10}$$

Since SHG and OPO are opposite interaction, their phase matching conditions are the same. With the fundamental frequency ω_r, the second harmonic or pump frequency ω_g and the index of refraction for the relevant polarization and frequency given by $n(\omega)$ the phase matching condition becomes

$$\Delta k = \frac{\omega_g n(\omega_g)}{c} - 2\left(\frac{\omega_r n(\omega_r)}{c}\right) - = 0 \tag{1.11}$$

From energy conservation we have $\omega_g = 2\omega_r$ so the phase matching condition is:

$$n(\omega_r) = n(\omega_g) \tag{1.12}$$

When the phase matching is not perfect, the strength of the nonlinear interaction depends on the mismatch: $\Delta k L_c$ L_c is the interaction length (the length of the crystal in which the fields interact). For second harmonic generation without pump depletion the second harmonic power produced is given by [6, ch 2]:

$$I(\Delta k L) = I_{max}\left(\frac{\sin \Delta k L_c/2}{\Delta k L_c/2}\right)^2 \tag{1.13}$$

where I_{max} is second harmonic power produced with perfect phase matching. Since low loss materials usually have normal dispersion, where the index of refraction is a monotonically increasing function of frequency, achieving good phase matching is one of the main challenges of working with nonlinear optics. There are different methods for achieving phase matching, most of which make use of a crystal's birefringence and use combinations of different polarizations that will have the right indexes of refraction for the needed frequencies of light. We need the signal and idler fields to interfere with each other to create quadrature squeezing, so we need a phase matching type in our OPO where the signal and idler fields have the same

polarization. We use a phase matching technique known as quasi-phase matching [6, 38, 46].

As illustrated in Figure 1-5 part B, when the phase matching is not perfect and there is a small mismatch Δk, the harmonic field amplitude begins to decrease after a distance called the coherence length of the interaction [6]. This is because the propagating harmonic field has become out of phase with the harmonic field that is being generated, and the interaction is transferring energy back to the fundamental field. In quasi- phase matching the direction of one crystal axis is switched (poled) periodically throughout the length of the crystal. This introduces a π phase shift to the generated harmonic beam. If the poling changes after one coherence length, as in Figure 1-5 part C, the interaction will always add energy to the generated field, and the generated field amplitude grows monotonically as the fields propagate through the crystal. Comparing part A and part C of Figure 1-5, it is clear that the effective nonlinearity is smaller for a quasi phase matching than it would be if the same crystal used perfect birefringent phase matching. In practice though, quasi-pahse matching allows us to use large nolinearities that can not be phase matched using birefringence, like the d_{33} nonlinearity in KTP, so the recent improvements in poling technology have made higher nonlinearities more easily accessible.

The condition on the poling period Λ is:

$$\Lambda = \frac{2\pi}{\Delta k} = \frac{\lambda_r}{2\left(n(\omega_g) - n(\omega_r)\right)} \tag{1.14}$$

where λ_r is the wavelength in vacuum of the fundamental field. In PPKTP we use the d_{33} nonlinearity, so the relevant index of refraction is along the polar (z) axis. Sellmeier equations for KTP are given in [25, 38, 41]. The index of refraction for 1064nm is 1.830 and for 532nm is 1.889, so the grating period is approximately 9 microns. The phase mismatch for quasi phase matching is given by:

$$L_c \Delta k' = 2\pi L_c \left(\frac{2}{\lambda_r} \left[n(\omega_g) - n(\omega_r) \right] + \frac{1}{\Lambda} \right) \tag{1.15}$$

The length of the crystal and the poling period both depend on the temperature of the crystal because of the crystal's thermal expansion, while the indices of refraction also depend on temperature. To find the first order temperature dependence we take the derivative [27]:

$$\frac{d(L_c\Delta k')}{dT} = 2\pi\left[\frac{dL_c}{dT}\left(\frac{2}{\lambda_r}\left[n(\omega_g) - n(\omega_r)\right] + \frac{1}{\Lambda}\right) + \frac{2L_c}{\lambda_r}\left(\frac{dn(\omega_g)}{dT} - \frac{dn(\omega_r)}{dT}\right) - \frac{L_c}{\Lambda^2}\frac{d\Lambda}{dT}\right] \tag{1.16}$$

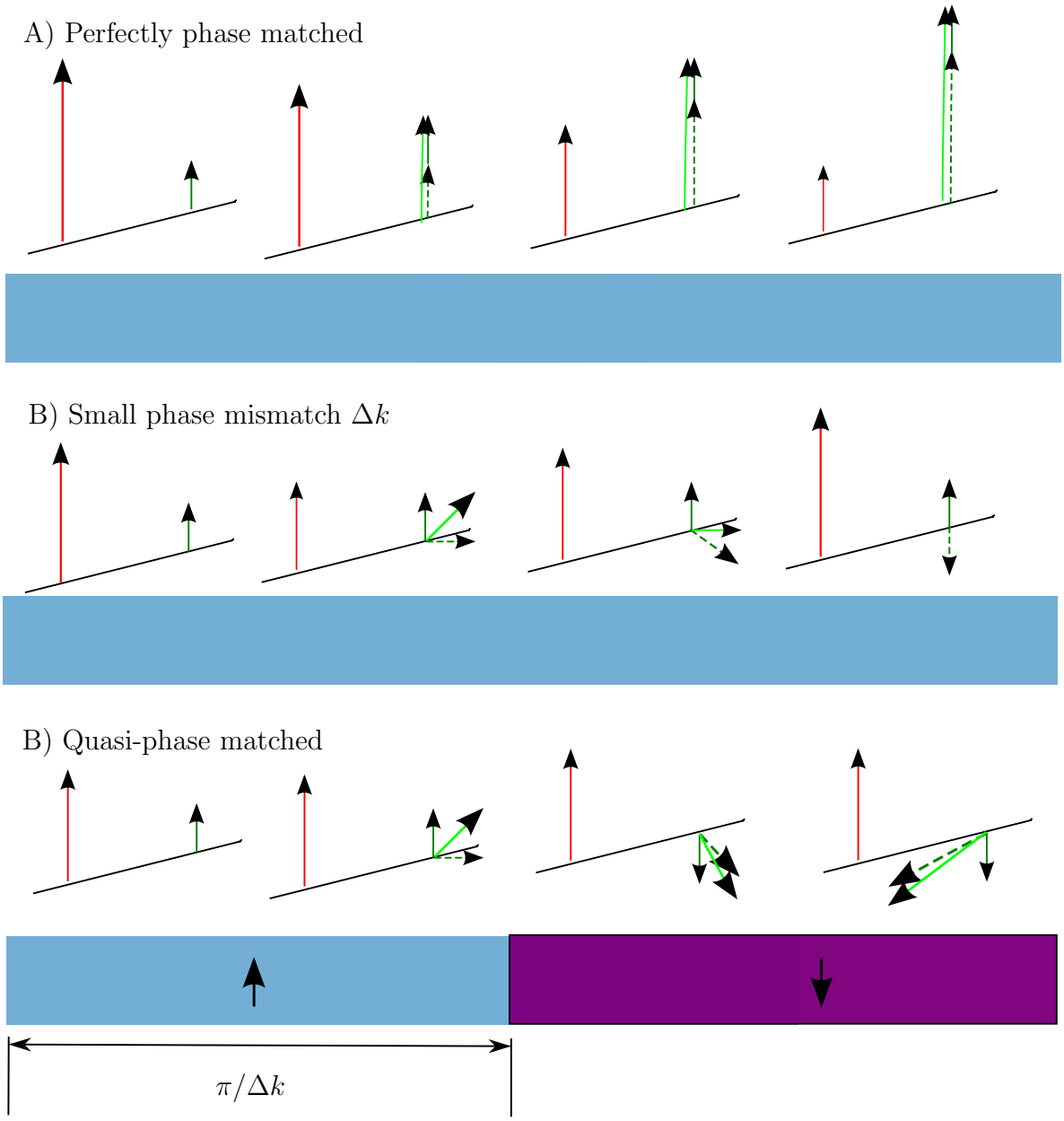

Figure 1-5: A) With perfect phase matching the generated harmonic field (dark green) stays in phase with the propagating harmonic field (dashed), so they add constructively and the total field (light green) grows monotonically. B) When there is a small phase mismatch, the propagating harmonic field acquires a phase shift relative to the fundamental as they propagate. After a distance of $\pi/\Delta k$ the generated harmonic field is out of phase with the propagating field and the harmonic field decreases until its amplitude is zero again at $2\pi/\Delta k$. C) In quasi phase matching, the crystal axis is reversed at $\pi/\Delta k$, or an integer multiple of that distance. This reverses the sign of the nonlinear coupling coefficient, so that there is a π phase shift to the generated field, and the interaction continues to add energy to the generated field. A periodically poled crystal is made up of many of these domains.

Thermal expansion of the lengths L_c and Λ is described by:

$$l(T) = l_0 \left[1 + \alpha(T - 25°C) + \beta(T - 25°C)^2\right] \tag{1.17}$$

where $\alpha = (6.7 \pm 0.7) \times 10^{-6}[1/°C]$ and $\beta = (11 \pm 2) \times 10^{-9}[1/°C^2]$, and l_0 is the length at room temperature [25]. Using the same equation for the total length, we get:

$$\frac{d(L_c \Delta k')}{dT} = 2k_r L_{c,0} \left(\alpha \left[n(\omega_g) - n(\omega_r)\right] + \frac{dn(\omega_g)}{dT} - \frac{dn(\omega_r)}{dT} \right) \tag{1.18}$$

where k_r is the wavenumber of the fundamental field in vacuum. In this first order approximation, the temperature dependence of the phase mismatch is independent of the poling period. An equation for the index of refraction of PPKTP as a function of wavelength and temperature is given in [25], we will use only the first derivatives with temperature:

$$\begin{aligned} \left.\frac{dn}{dT}\right|_{1064nm,25°C} &= 1.4774 \times 10^{-5}[1/°C] \\ \left.\frac{dn}{dT}\right|_{532nm,25°C} &= 2.4188 \times 10^{-5}[1/°C] \end{aligned} \tag{1.19}$$

The phase mismatch, expanded around the peak of the phase matching curve is given by:

$$L_c \Delta k' = 2k_r L_c \left(\alpha \left[n(\omega_g) - n(\omega_r)\right] + \frac{dn(\omega_g)}{dT} - \frac{dn(\omega_r)}{dT} \right) (T - T_0) \tag{1.20}$$

where T_0 is the phase matching temperature. Figure 1-6 shows a measurement of the efficiency of second harmonic generation (in single pass) over a range of crystal temperatures. This measurement was made in single pass to avoid pump depletion and thermal effects present in SHG inside of a cavity, so the resulting curve is in agreement with Equation 1.13.

1.2.3 OPO: Resonant for pump

Our OPO is based on a design from the Australian National University. Our OPO is resonant for both the fundamental and second harmonic field, unlike many OPO's used for squeezing

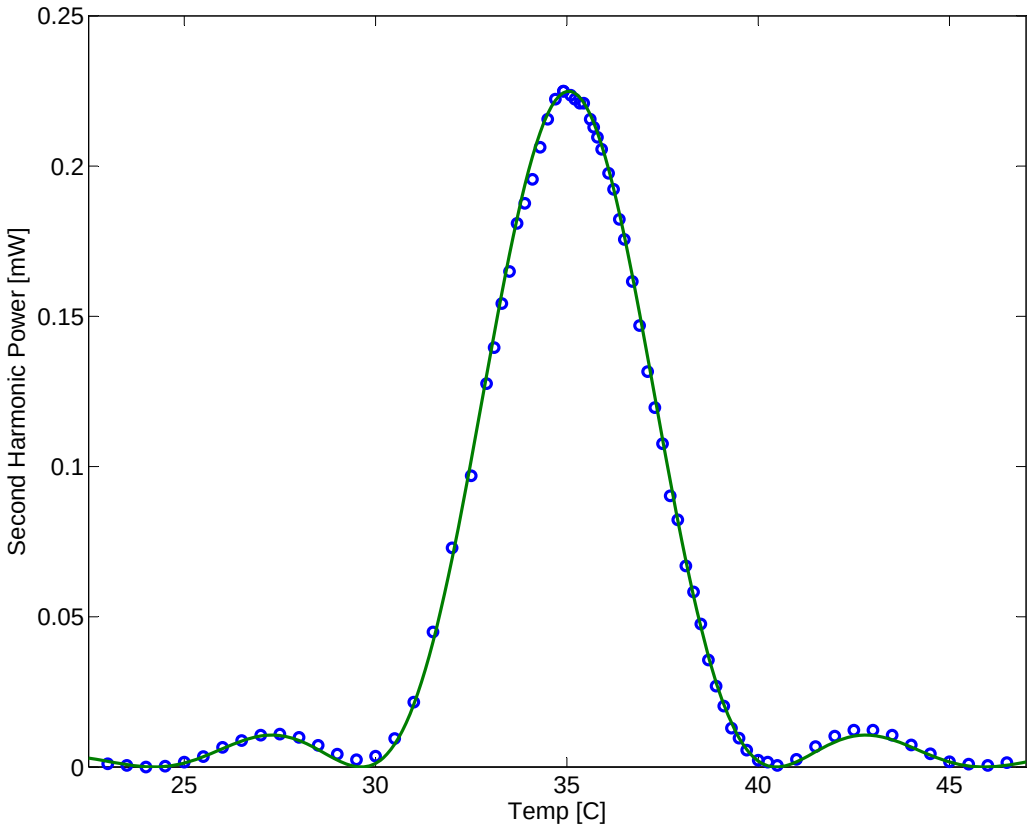

Figure 1-6: Single pass second harmonic generation with PPKTP, with 333mW of incident infrared power. The green curves is a prediction based on 1.18 and literature values for index of refraction and thermal expansion. The peak height is normalized to fit the data, and the location of the center is set to match the data.

which are resonant for the fundamental field only [69]. We can use the second harmonic pump field to lock the length of the OPO with a Pound-Drever-Hall locking scheme and do not need an additional field at the fundamental frequency to sense the cavity length. Because our OPO resonantly enhances the green field, the incident pump power needed to reach threshold is lower than it would be if the pump were single pass. A resonant OPO acts as a filter for high frequency fluctuations of the second harmonic field, although the linewidth is wide and so only high frequency fluctuations are filtered. An external mode cleaner cavity can also accomplish this filtering, with a narrower linewidth [51]. The resonant cavity also acts as a filter on the spatial mode inside the OPO. To maximize the nonlinear interaction the crystal is placed at the focus of the cavity mode. The second harmonic field in a cavity mode with waist w_0 interacts with the fundamental field in the cavity mode with a waist $\sqrt{2}w_0$. In an empty cavity or an OPO using birefringent phase matching, these modes would be exactly the modes that resonate in the cavity. For a useful discussion of the propagation of Gaussian beams in a nonlinear cavity, see [38, 2.4.8]. Because we use quasi phase matched cavity, there is a small difference in the waist sizes caused by the difference in the index of refraction for 532nm and 1064nm, but this difference is small compared to the mode matching errors that could be present without a resonant cavity. Because we use the pump field to lock the length of the cavity, we need to ensure that the cavity is resonant for the red field when it is locked to the green field 1.2.4. This places more stringent requirements on the temperature stability of an OPO that is resonant for the pump, as will be discussed in Chapter **??**. Using a cavity that is resonant for the pump, and locking the length with the pump field simplifies our experimental set-up, and lowers the required green power, but doesn't have any significant performance advantage over an OPO that is resonant for the fundamental field only.

1.2.4 OPO: Dispersion compensation

Because our cavity is resonant for the red and green field, and locked using the green field, we need to make sure that the cavity is resonant for red when it is resonant for green, or no

squeezing will be produced. This places a more stringent requirement on the temperature stability of the crystal than the phase matching condition. This is a problem specific to low frequency squeezers, not only to squeezers length locked using the second harmonic field. To produce squeezing at low frequencies, no coherent field can enter the cavity mode that is to be squeezed without adding classical noise which will mask the squeezing, so light in a different mode must be used to sens the cavity length for locking. In an OPO that is not resonant for the pump, an infrared field that is shifted in frequency and rotated in polarization from the squeezed field is used to lock the cavity length. In this case the polarization rotated beam must be co-resonant with the squeezed polarization [43], a very similar situation to the co-resonance condition for the harmonic and fundamental fields.

The resonance condition for a cavity is that the phase acquired in one round trip must be an integral multiple of 2π for a field to resonate. For the red and green fields in the OPO this can be written:

$$\phi_{r,rt} = k_r \left[L + (n(\omega_r) - 1)\, L_{c,tot}\right] + \phi_{r,m} = 2\pi m_1 \tag{1.21}$$

$$\phi_{g,rt} = k_g \left[L + (n(\omega_g) - 1)\, L_{c,tot}\right] + \phi_{g,m} = 2\pi m_2 \tag{1.22}$$

where L is total cavity length, $L_{c,tot}$ is total the length of the crystal, $\phi_{r,m}, \phi_{g,m}$ is the sum of the phase shifts from reflection off of each cavity mirror for the red and green fields, k_r and k_g are the wavenumbers in vacuum, and m_1, m_2 are integers. The mirror phase shifts can be different for the two wavelengths, and because we are using quasi-phase matching, the index of refraction is also different for the two wavelengths. Because $k_g = 2k_r$ there are twice as many cavity lengths that satisfy 1.22 as 1.21. The Pound-Drever-Hall lock will adjust the total cavity length to ensure that the condition 1.22 is met, but that does not guarantee that 1.21 will be satisfied. The condition imposed by the Pound Drever Hall lock is:

$$L = \frac{2\pi m_2 - \phi_{g,m}}{2k_r} - (n(\omega_g) - 1)L_{c,tot} \tag{1.23}$$

With this cavity length the condition 1.21 is violated by an amount

$$\Delta\phi_{rt} = \phi_{r,m} - \frac{\phi_{g,m}}{2} + [n(\omega_r) - n(\omega_g)]\, k_r L_{c,tot} \tag{1.24}$$

if m_2 is an even number, or $\pi + \Delta\phi_{r,rt}$ is m_1 is an odd number, and k_r is the wavenumber of the fundamental field in a vacuum. To compensate for this phase shift, we need to introduce an adjustable phase shift into the cavity, called dispersion compensation. One method would be to put an additional dispersive medium which would have different indices for the fundamental and harmonic fields, with an adjustable length. This could be done with a antireflection coated flat piece of glass called a dispersion plate, which could be rotated to adjust the path length, which has the disadvantage of adding additional losses and scatter into the cavity. The dependence of the phase shift on the crystal temperature is given by 1.17 and 1.19 and the derivative:

$$\begin{aligned} \frac{d\Delta\phi_{rt}}{dT} &= k_r L_{c,tot} \left(\alpha[n(\omega_r) - n(\omega_g)] + \left[\frac{dn(\omega_r)}{dT} - \frac{dn(\omega_g)}{dT} \right] \right) \\ &= \frac{-1}{2} \frac{d(L_c \Delta k')}{dT} \end{aligned} \tag{1.25}$$

which is half the temperature dependence of the phase mismatch, assuming that the total crystal length is approximately the same as the poled length of the crystal.

As shown in Figure 1-7, co-resonance does not necessarily occur at the same temperature as the peak of the phase matching curve. To produce strong squeezing our OPO needs to be well phase matched and co-resonant. We could adjust the temperature to meet one of those conditions, but not both. We use the crystal temperature to set the phase matching, and adjust the crystal length to ensure co-resonance. At any temperature, co-resonance occurs when the crystal length is:

$$L_{c,tot} = \frac{(2\pi m + \phi_{g,m}/2 - \phi_{r,m})}{k_r[n(\omega_r) - n(\omega_g)]} \tag{1.26}$$

where m is an integer. A wedged crystal, like the one shown in Figure 1-8, mounted on a

translation stage, allows us to adjust the crystal length once it is already installed in the cavity [40]. At one edge of the crystal the poling stops, and the edge is polished with a wedge. The nonlinear interaction in this part of the crystal is not efficient, since there is no poling, but we can translate the crystal horizontally in the cavity to find a location in the cavity where there is co-resonance for any temperature. The wedge angle is small ($\theta_w = 1.43°$ in our crystal) so the total crystal length is given by:

$$L_{c,tot} = L_c + y \sin \theta_w \tag{1.27}$$

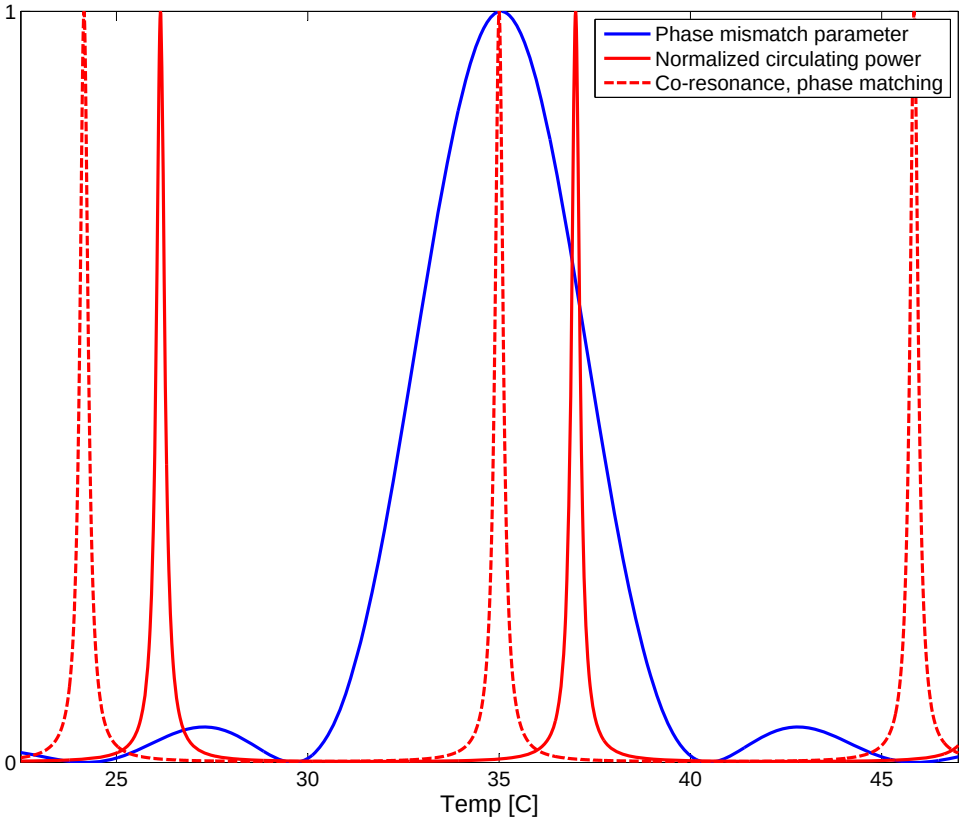

Figure 1-7: Temperature dependence of phase matching and dispersion compensation. The blue curve is the phase mismatch parameter, $\mathrm{sinc}^2 \Delta k' L_c$ for PPKTP phase matched at $35°C$. The red curves are calculated assuming that the cavity is locked using the 532nm pump field, and shows the normalized transmission profile of our OPO for 1064nm as a function of temperature. The location of the resonance peak relative to the phase matching peak depends on the dispersion of the cavity optics. The dashed red line represents the ideal situation, where the red resonance peak is at the phase matching peak.

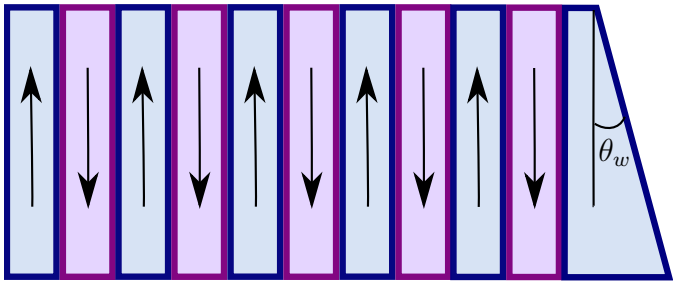

Figure 1-8: Wedged periodically poled crystal

where L_c is the poled length of the crystal where the interaction is quasi phase matched, and y is the crystal displacement measured from the shorter edge. The dependence of the dispersion mismatch on crystal position is given by:

$$\frac{d\Delta\phi_{rt}}{dy} = (n(\omega_r) - n(\omega_g))\, k_r \sin\theta_w \tag{1.28}$$

Since we can adjust the total crystal length by about $125\mu m$, there are approximately 10 locations in the crystal where the cavity could be co-resonant at any temperature. Since we need to avoid clipping the beams on the edges of the crystal in practice there are around 3-5 usable locations in the crystal where the the cavity is co-resonant at a certain temperature. There are occasionally defects in the crystal that lead to higher losses or lower interaction strength at one of these crystal positions. As a function of crystal position and temperature the dispersion mismatch is given by:

$$\begin{aligned}\Delta\phi_{rt} = \phi_{r,m} - \frac{\phi_{g,m}}{2} + k_r \left[n(\omega_r) - n(\omega_g) + \left(\frac{dn(\omega_r)}{dT} - \frac{dn(\omega_g)}{dT} \right) (T - 25°C) \right] \\ \times (L_c + y \sin\theta_w)\,(1 + \alpha(T - 25°C)) \qquad (1.29) \\ \approx k_r \left(\frac{dn(\omega_r)}{dT} - \frac{dn(\omega_g)}{dT} + \alpha[n(\omega_r) - n(\omega_g)] \right) L_c (T - T_0) \\ + k_r [n(\omega_r) - n(\omega_g)] \sin\theta_w (y - y_0) \qquad (1.30)\end{aligned}$$

where in the approximation T_0 is the phase matching temperature and y_0 is the position where the cavity is co-resonant at the phase matching temperature. Using 1.20 the dispersion

mismatch in terms of the phase mismatch is:

$$\Delta\phi_{rt} = -\frac{\Delta k' L_c}{2} + k_r[n(\omega_r) - n(\omega_g)]\sin\theta_w(y - y_0) \tag{1.31}$$

Then the crystal position where the cavity is co-resonant for a particular temperature is given by:

$$y_{cr} = -\frac{\Delta k' L_c}{2k_r[n(\omega_g) - n(\omega_r)]\sin\theta_w} + y_o \tag{1.32}$$

1.2.5 Classical OPO: nonlinear gain and threshold

The classical dynamics of an OPO, developed in [19], can be used to characterize the strength of the nonlinear interaction. One advantage of an OPO resonant for the pump field is the lower pump power needed to reach a particular value of the normalized nonlinear interaction strength x. The OPO reaches threshold when the red power generated from interaction with the pump and the power lost through cavity losses in each round trip are the same, above this pump power the cavity produces a coherent field at the fundamental frequency even when no seed beam at that frequency is present. The normalized nonlinear interaction strength from Section **??** is the ratio of gain to losses for the amplitude of the fundamental field, this ratio is one at threshold:

$$x_{th} = \frac{\epsilon|b|_{th}}{\gamma_r^{tot}} = 1 \tag{1.33}$$

Because the circulating pump power is proportional to the incident pump power, we can use equation 1.33 to write an alternative expression for the normalized nonlinear interaction strength:

$$x = \frac{\epsilon|b|_{th}}{\gamma_r^{tot}}\frac{|b|}{|b|_{th}} = \sqrt{\frac{P}{P_{th}}} \tag{1.34}$$

Although we operate the OPO below threshold, we normally use a significant fraction of

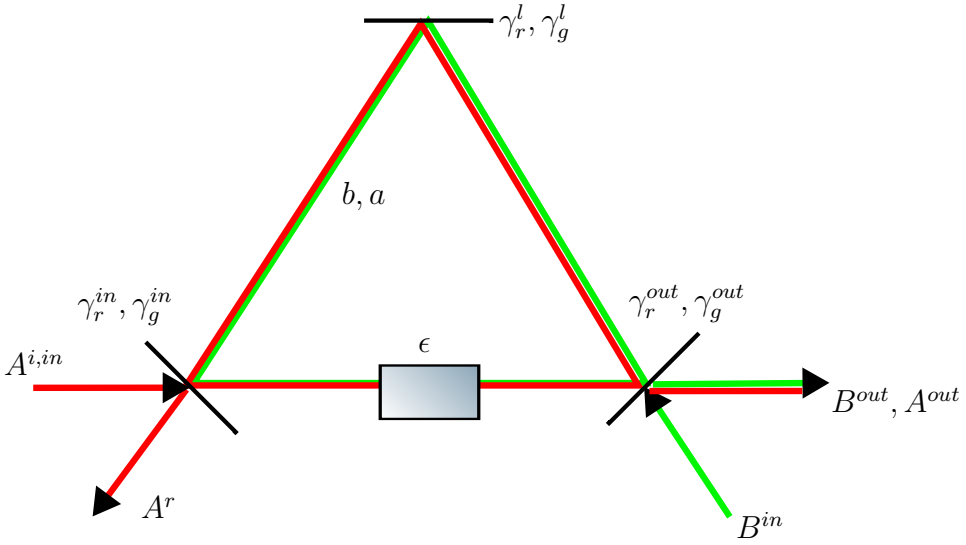

Figure 1-9: Classical OPO with seed. The rear coupler has decay rates γ_r^{in} and γ_g^{in}. In **??** these decay rates were inclded in the intracavity loss decay rates γ_r^l and γ_g^l but here they will be treated separately.

the threshold power to pump the OPO, so we can set a requirement on the available second harmonic power using the threshold power.

The cavity equations of motion for a degenerate OPO are the same as the equations for SHG, with coherent driving fields at both the fundamental and second harmonic frequencies:

$$\dot{a}(t) = -(\gamma_r^{tot} - i\Delta_a(t))a(t) + \epsilon a^\dagger(t)b(t) + \sqrt{2\gamma_r^{in}}A^{in} \tag{1.35}$$

$$\dot{b}(t) = -(\gamma_g^{tot} - i\Delta_b(t))b(t) - \frac{\epsilon a^2(t)}{2} + \sqrt{2\gamma_g^{out}}B^{in} \tag{1.36}$$

We have again left out quantum fluctuations. We will assume that the cavity is on resonance for the both the pump and seed fields and let both of the detunings Δ_a and Δ_b go to zero. As illustrated in Figure 1-9, the incident green field B^{in} couples into the cavity through the output coupler with decay rate γ_g^{out} while the incident seed field A^{in} couples through the rear coupler with decay rate γ_r^{in}. We will also make the approximation again that the pump field is not depleted, so that we can drop the second term from Equation 1.36. In the steady

state where the field amplitudes are constant these equations become:

$$0 = -\gamma_r^{tot} a + \epsilon a^\dagger b + \sqrt{2\gamma_r^{in}} A^{in} \tag{1.37}$$

$$b = \frac{\sqrt{2\gamma_g^{out}}}{\gamma_g^{tot}} B^{in} \tag{1.38}$$

Combining the threshold condition 1.33and 1.38 we can find a value for the incident pump power needed to reach threshold:

$$P_{th} = \hbar\omega_g \left|B^{in}\right|^2 = \frac{\hbar\omega_g \left(\gamma_r^{tot}\gamma_g^{tot}\right)^2}{2\epsilon^2\gamma_g^{in}} \tag{1.39}$$

$$\approx \frac{\hbar\omega_g(\gamma_r^{tot})^2\gamma_g^{tot}}{2\epsilon^2} \tag{1.40}$$

where we made the approximation that $\gamma_g^{tot} = \gamma_g^{tot}$. One simple way to measure the threshold is to increase the pump power until a red beam is produced, this gives a rough idea of the threshold power. A more accurate method is to measure the classical nonlinear amplification and de-amplification as a function of the pump power. Measurements of the classical nonlinear gain are also the best way to estimate the normalized nonlinear interaction strength, x.

To calculate the nonlinear gain we can set the relative phases so that the incident seed is real, and solve Equation 1.37 and its complex conjugate for the circulating red field. Using the input output relation we find the output field $A^{out} = \sqrt{2\gamma_r^{out}}a$ [75].

$$A^{out} = \frac{2\sqrt{\gamma_r^{out}\gamma_r^{in}}}{\gamma_r^{tot}} \frac{1 + xe^{i\phi}}{1 - x^2} A^{in} \tag{1.41}$$

where ϕ is again the phase of the circulating pump. The parametric gain is the ratio of the

output power to the output power with no pump present:

$$G(x,\phi) = \frac{1 + 2x\cos\phi + x^2}{(1-x^2)^2} \tag{1.42}$$

$$G(x,0) = \frac{1}{(1-x)^2} \tag{1.43}$$

$$G(x,\pi) = \frac{1}{(1+x)^2} = g \tag{1.44}$$

Where 1.43 describes parametric de-amplification and 1.44 describes amplification. We measure the nonlinear gain by loacking the cavity with the green field, and sending a small amount of light from the pump laser (the seed) enter the cavity through the rear coupler. We then scan the phase of either the seed or the pump field and measure the maximum transmitted power. This is compared to the power transmitted when scanning the cavity with only the seed injected. As shown in Figure 1-10 the threshold for our OPO was near 95mW. This value increased by about 10% over the course of a year, this may be due to a slow drift in crystal position.

When setting the pump power and the crystal temperature we measure the parametric gain g, to find the value of the normalized nonlinear interaction strength:

$$x = 1 - 1/\sqrt{G(x,\pi)} = 1 - 1/\sqrt{g} \tag{1.45}$$

Since the parametric gain depends on careful tunning of the crystal temperature, we monitor the parametric gain to adjust the crystal temperature. One could also estimate the normalized nonlinear interaction strength by measuring the power incident on the OPO, using Equation 1.34. This has the disadvantage that misalignment or mode mismatch of the pump beam, errors in the temperature setting, or a drift in the threshold power will all cause errors in the estimate of the normalized interaction strength.

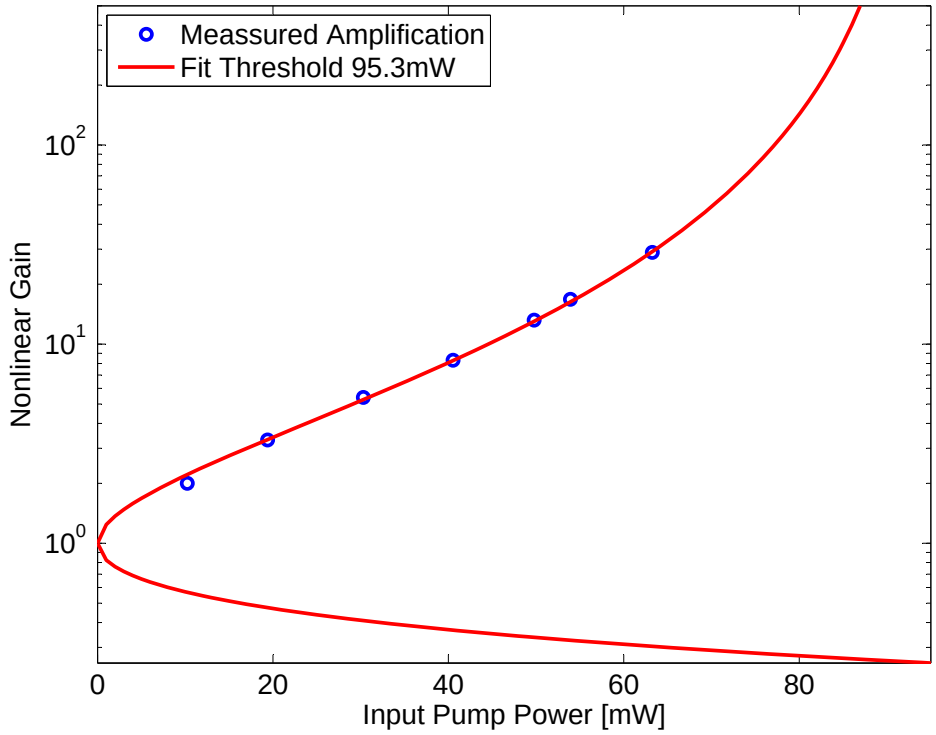

Figure 1-10: Parametric amplification as a function of green power, used to find a value for the threshold of oscillation. Amplification is used because small offsets make larger errors in measurements of deamplification. As the pump power approaches threshold the amplification approaches an asymptote.

1.2.6 Optimizing nonlinear interaction strength: Phase matching and dispersion compensation in an OPO resonant for the pump

To get the best squeezing we need to operate our OPO at the peak of the phase matching and on co-resonance. We can achieve this by maximizing the classical nonlinear gain (and therefore the normalized nonlinear interaction strength) for a fixed pump power. The effect of a phase mismatch is to change the nonlinear coupling constant, which becomes complex [39]:

$$x' = xe^{i\Delta k' L_c/2}\,\mathrm{sinc}(\Delta k' L_c/2) \tag{1.46}$$

where x is the same as defined in **??**(check this is right!). We can write the normalized nonlinear interaction strength as $|x'|e^{i(\phi_p+\Delta k' L_c/2)}$ If the co-resonance condition is not satisfied, a detuning is introduced to the fundamental field:

$$\Delta_a = \frac{\Delta\phi_{rt}}{\tau} \tag{1.47}$$

With a detuning and a complex value of x included, Equation 1.35 and its complex conjugate become:

$$\begin{pmatrix} 0 \\ 0 \end{pmatrix} = \gamma_r^{tot} \begin{pmatrix} 1 - i\Delta_a/\gamma_r^{tot} & |x'|e^{i(\phi_p+\Delta k' L_c/2)} \\ |x'|e^{-i(\phi_p+\Delta k' L_c/2)} & 1 - i\Delta_a/\gamma_r^{tot} \end{pmatrix} \begin{pmatrix} a \\ a^\dagger \end{pmatrix} + \sqrt{2\gamma_r^{tot}} \begin{pmatrix} A^{in} \\ A^{in*} \end{pmatrix} \tag{1.48}$$

Setting the input seed phase to zero again we find the output field:

$$A^{out} = \frac{2\sqrt{\gamma_r^{out}\gamma_r^{in}}}{\gamma_r^{tot}} \frac{1 + i\Delta_a/\gamma_r^{tot} + |x'|e^{i(\phi_p+\Delta k' L_c/2)}}{1 + (\Delta/\gamma_r^{tot})^2 - |x'|^2} A^{in} \tag{1.49}$$

The parametric amplification is given by:

$$G = \frac{1 + \left(\frac{\Delta_a}{\gamma_r^{tot}}\right)^2}{\left(1 + (\Delta_a/\gamma_r^{tot})^2 - |x'|^2\right)^2} \left| 1 + i\frac{\Delta_a}{\gamma_r^{tot}} + |x'|e^{i(\phi_p+\Delta k' L_c/2)} \right|^2 \tag{1.50}$$

The parametric gain is maximized when

$$\phi_p + \frac{\Delta k' L_c}{2} = \tan^{-1} \frac{\Delta_a}{\gamma_r^{tot}} \tag{1.51}$$

The maximum classical gain we measure then is given by:

$$G_m = \left(1 - \frac{|x'|}{\sqrt{1 + \left(\Delta_a/\gamma_r^{tot}\right)^2}} \right)^{-2} \tag{1.52}$$

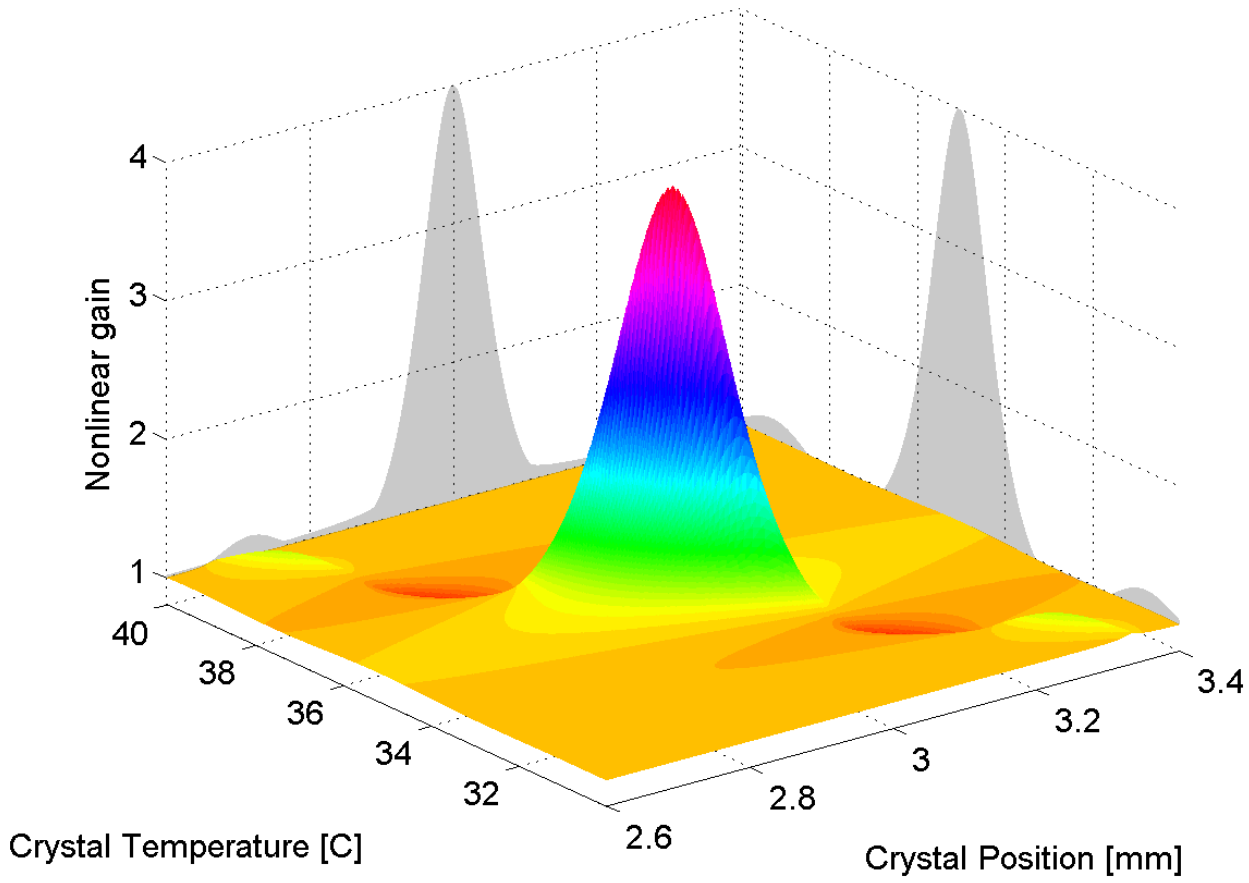

Figure 1-11: Non linear gain as a function of crystal position and temperature for our OPO parameters, and a pump power at one quarter of the threshold value. This pattern is repeated a few times across the width of the crystal, at the same temperatures. The projection on the position axis shows the maximum gain that can be measured at each crystal position once the temperature is optimized.

Since γ_r^{tot} is the half width at half maximum in angular units, the red cavity finesse is $\mathcal{F}_r = \pi/(\tau\gamma_r^{tot})$.

$$G_m = \left(1 - \frac{x\,\mathrm{sinc}(\Delta k' L_c/2)}{\sqrt{1 + (\mathcal{F}_r \Delta\phi_{rt}/\pi)^2}}\right)^{-2} \tag{1.53}$$

Figure 1-11 shows the nonlinear gain as a function of crystal position and temperature

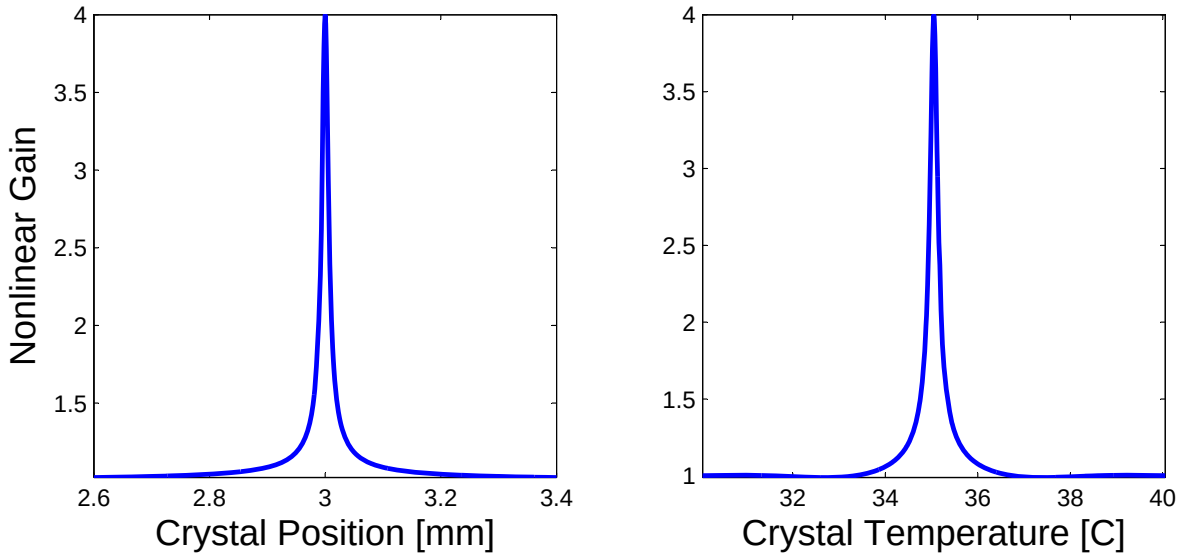

Figure 1-12: Gain profiles with crystal position and temperature. The left panel shows a cross section of the nonlinear gain when the temperature is set to the phase matching temperature (chosen to be $35°C$ for this example) and the position is varied. The right panel shows a cross section of gain with temperature when the crystal position is set for co-resonance at the phase matching temperature (chosen to be 3mm).

for the parameters of our OPO. A practical procedure for finding the best crystal position is described in Appendix B. The dispersion mismatch $\Delta\phi_{rt}$ is scaled by the red cavity finesse, which gives us another factor to consider where choosing the cavity finesse, since the requirement for temperature stability (and accurate crystal placement) will become more stringent as we increase the red finesse. Figure 1-12 shows profiles of the dependence of nonlinear gain on crystal position and temperature around the point where gain is maximized, with the same parameters as Figure 1-11.

1.2.7 OPO: Escape efficiency

When choosing the input coupler reflectivity for an OPO and therefore the cavity finesse, the most important factor to consider is the escape efficiency, in addition to the requirements for pump power and temperature stability discussed above. As was shown in **??** a lower escape efficiency directly lowers the amount of squeezing produced. The escape efficiency can be

written in the limit of a low loss cavity as:

$$\eta_{esc} = \frac{\gamma_r^{out}}{\gamma_r^{tot}} \tag{1.54}$$

$$= \frac{T_{out}}{T_{out} + L_{cav}} \tag{1.55}$$

where T_{out} is the output coupler infrared power transmission and L_{cav} is the infrared intra-cavity power losses. We measured the intra-cavity losses for our OPO by injecting an infrared field into the input coupler and scanning the cavity through resonance while measuring the reflected power. The ratio of the reflected power on resonance to off resonance is given by [23]:

$$\frac{I_{r,on}}{I_{r,off}} = \frac{\left| \frac{r_{out} - r_l}{1 - r_{out} r_l} \right|^2}{\left| \frac{r_{out} + r_l}{1 + r_{out} r_l} \right|^2} \tag{1.56}$$

where $r_{out} = \sqrt{1 - T_{out}}$ and $r_l = \sqrt{1 - L_{cav}}$. This measurement showed that we had an intra-cavity loss of 0.43% without the crystal installed, this includes a loss of 0.18% from the coupler for the control field, and two high reflectors with 0.05% losses, so the unaccounted for intra cavity losses are 0.2%. With the superpolished crystal used in the final configuration the crystal losses were 0.16%, and the total intracavity losses were 0.58%. With our input coupler power transmission of 13.24%, our OPO escape efficiency was 95.9%. Either lowering the intracavity losses or increasing the output coupler reflectivity would increase the escape efficiency. In practice it may be easier to increase the transmission of the output coupler and lower the cavity finesse than to further reduce the intra-cavity losses.

1.2.8 OPO: Traveling wave cavity

When implementing squeezing on a full scale gravitational wave detector we need to avoid adding technical noise to the interferometer, which is the subject of chapter **??**. A small amount of light will be scattered from the interferometer towards the squeezer, and if the

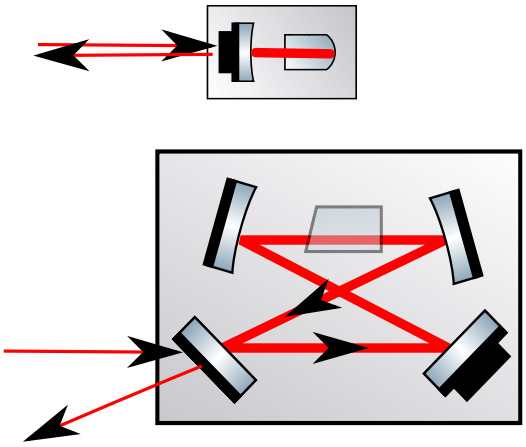

Figure 1-13: Standing wave (top) and traveling wave (bottom) cavity configurations

squeezer reflects this light back towards the interferometer it will degrade the interferometer sensitivity as explained in Section **??**. In order to keep the escape efficiency of an OPO large, it must be an over-coupled cavity. This means that the output coupler is the dominant loss in the cavity, and that the reflectivity of the cavity to any light incident on the input coupler is nearly unity. This means that most stray light from the interferometer that is incident on the OPO will be reflected off the input coupler, either directly reflected or after circulating in the cavity and leaking out of the input coupler. As shown in Figure 1-13 in a standing wave OPO any light incident on the input coupler from the interferometer will be reflected back towards the interferometer. The power in the stray beam can be attenuated using a series of Faraday isolators in the path used to inject squeezing into the interferometer, however the loss introduced by each additional Faraday isolator degrades the squeezing. In a traveling wave design stray light from the interferometer will be also be reflected off of the output coupler, but it will not be directed back towards the interferometer. When constructing the path for the green light entering the OPO, it is useful to keep in mind that stray light from the interferometer will counter-propagate along this path and take care to minimize the amount of stray light that is back-reflected. Even in the traveling wave configuration a small amount of the circulating power in the OPO is scattered by imperfections of the cavity optics into the couter-propagating mode, so that it will be scattered back towards the interferometer. This effect was measured in an OPO very similar to ours in [12], and will be

discussed further in **??**.

A traveling wave cavity also introduces a small amount of astigmatism into the squeezed beam, which will cause a small amount of loss due to imperfect mode matching. In Enhanced LIGO the astigmatism of the anti-symmetric port beam was much larger, so this was not a limit to the observed squeezing. A traveling wave cavity can be less mechanically stable than a standing wave cavity which can be made compact, the length stability of the OPO could become a limit to the observed squeezing as discussed in Chapter **??**.

1.2.9 Complete squeezer layout

There are several details of the squeezer design that were left out of Figure 1-3 for clarity, but are useful for practical operation. A more complete diagram of the experiment is shown in Figure 1-14.

To prevent any of light at the fundamental frequency from entering the OPO through the pump path, we use several dichroics to clean residual infared photons out of that beam. A Mach-Zender interferometer in the pump path allows us to intensity stabilize the pump, this reduces thermal fluctuations in the crystal which will limit the long term stability of the squeezer but was not needed for our experiment.

There are a few features that are useful for tuning the performance of the diagnostic balanced homodyne, using the on table local oscillator from the pump laser. The common mode rejection of the local oscillator port on the balanced homodyne detector can be checked and adjusted using the EOM in the on table LO path as an amplitude modulator. The homodyne visibility can be adjusted using the interference of the seed beam with the on table local oscillator with matched powers. The seed beam enters the OPO through the rear coupler and is blocked during normal operation. To measure the homodyne fringe visibility the OPO temperature is moved away from phase matching, and a filter is inserted in the green path to lower the power so that there will be no nonlinear gain in the OPO and the transmitted seed power will be stable. The transmitted beam, or the transmitted control beam, can also be used for aligning the interferometer injection path.

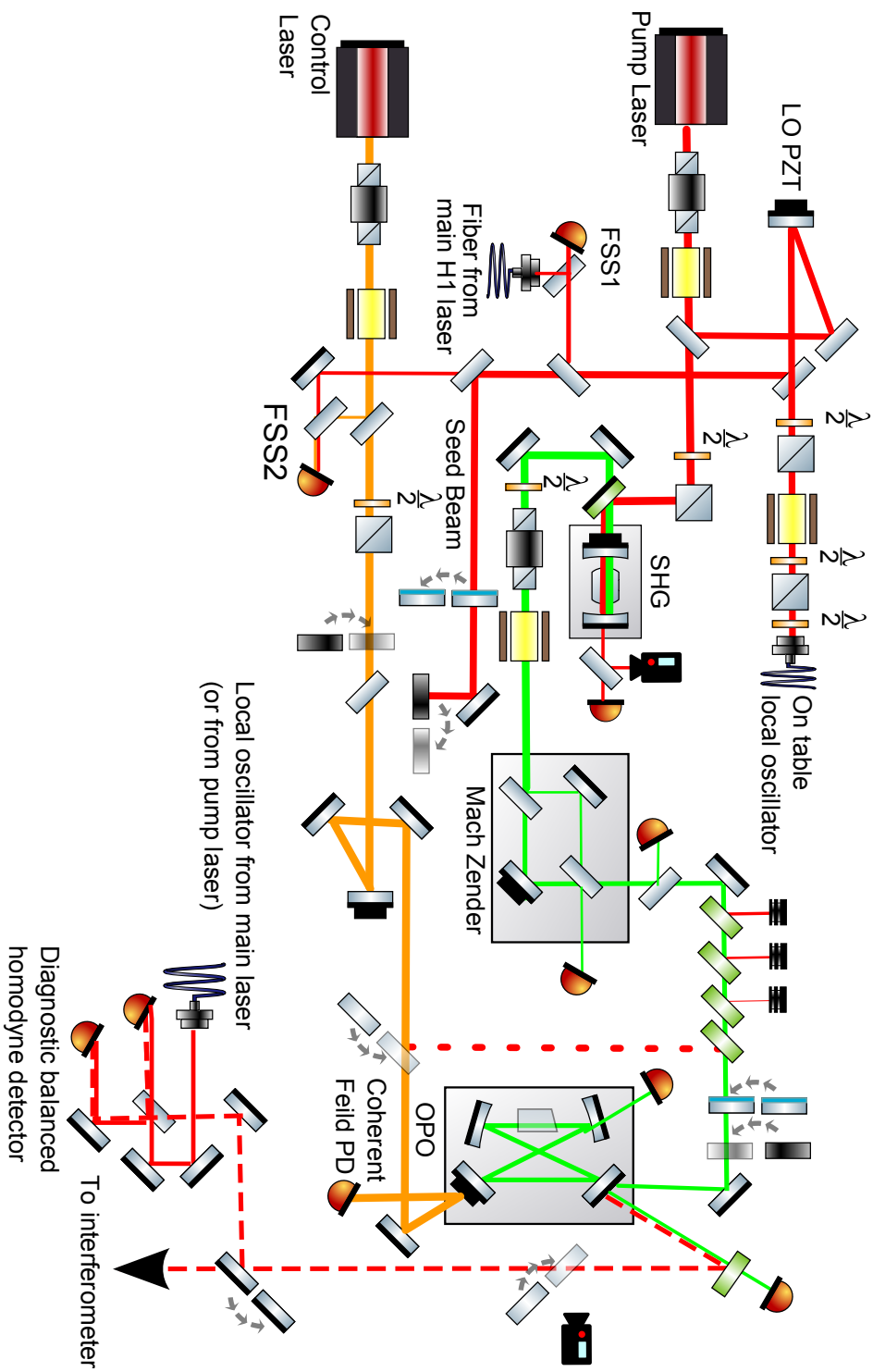

Figure 1-14: Layout of squeezed state source

There is also the option of injecting the seed beam into the OPO through the input coupler, this path is shown by a dashed line in Figure 1-14. This allows us to measure the intracavity loss, which may change depending on the crystal position. If the threshold power changes, a measurement of the intra-cavity loss can help diagnose the cause. If the forward seed is well mode-matched it can also be used as a rough alignment beam which has higher power than the transmitted alignment beams, useful for finding the beam in the initial alignment into the interferometer.

1.2.10 Squeezer performance

Our squeezer met the requirements of this experiment. Figure 1-15 shows the squeezing measured on the diagnostic homodyne detector. In the kHz range, we measured 6dB of squeezing, and 5dB at 100 Hz. The level of squeezing was shown to be stable for at an hour and a half. Using the propagation losses in our detection path, we estimate around 10dB of squeezing produced right outside the input coupler. To allow operation from the control room, the squeezer was connected to LIGO's digital slow control system.

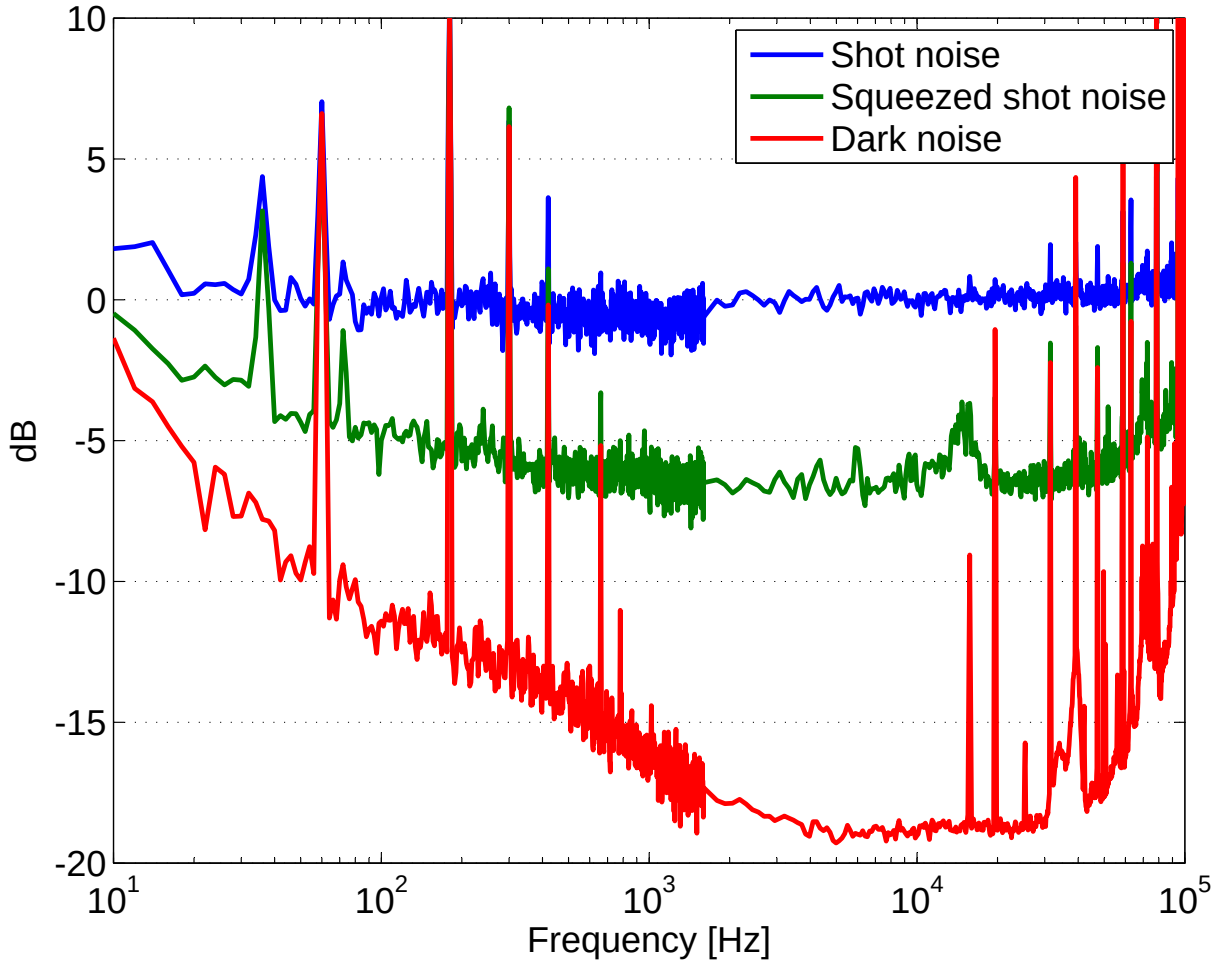

Figure 1-15: Squeezing measured on diagnostic homodyne detector. The red trace shows the electronics noise of the detector.

1.3 Squeezed state injection into Enhanced LIGO

Figure 1-16 shows a schematic of the squeezing injection into Enhanced LIGO. The squeezed state source was outside of the vacuum system on an optical table bolted to the ground. An extra Faraday isolator was added inside of vacuum in the squeezing injection path, to prevent stray light from the interferometer from reaching the squeezer and being back-reflected. After reflection off of the arm cavities the squeezed beam co-propagates with the interferometer beam, towards the anti-symmetric port. An added photo-diode on the AS

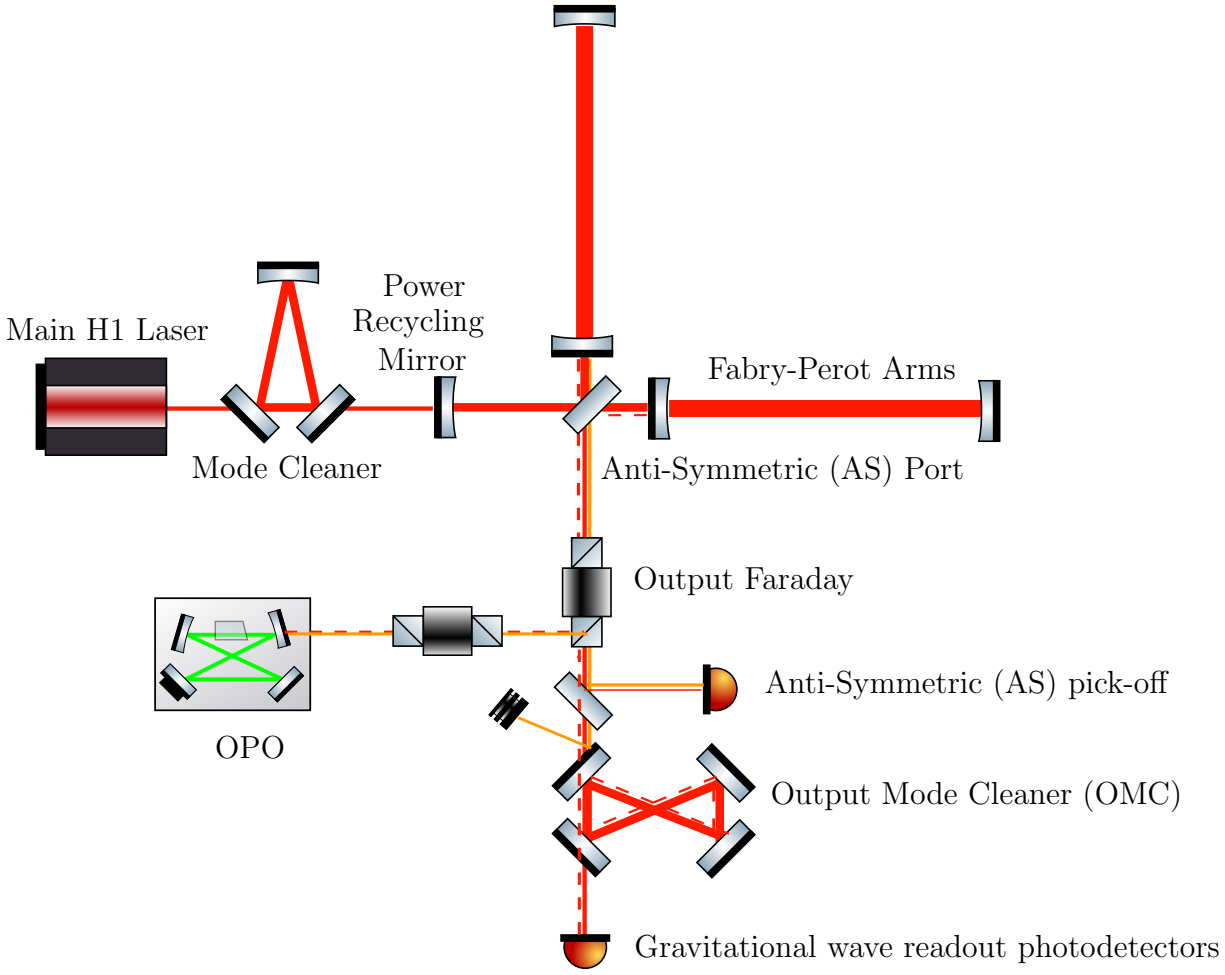

Figure 1-16: Squeezing injection into Enhanced LIGO

table senses the phase between the interferometer carrier beams and the control sidebands on the squeezed beam. The OMC reflects the squeezer control sidebands, and transmits the interferometer carrier and the squeezing to the gravitational wave readout photo-detectors where the improvement in sensitivity is measured.

1.3.1 Sensitivity improvement

Figure 1-17 shows a comparison of the calibrated sensitivity with squeezing injected and a reference of the calibrated sensitivity without squeezing. This is 2dB of noise reduction in the region around 2 kHz and there is some improvement from squeezing down to 140 Hz.

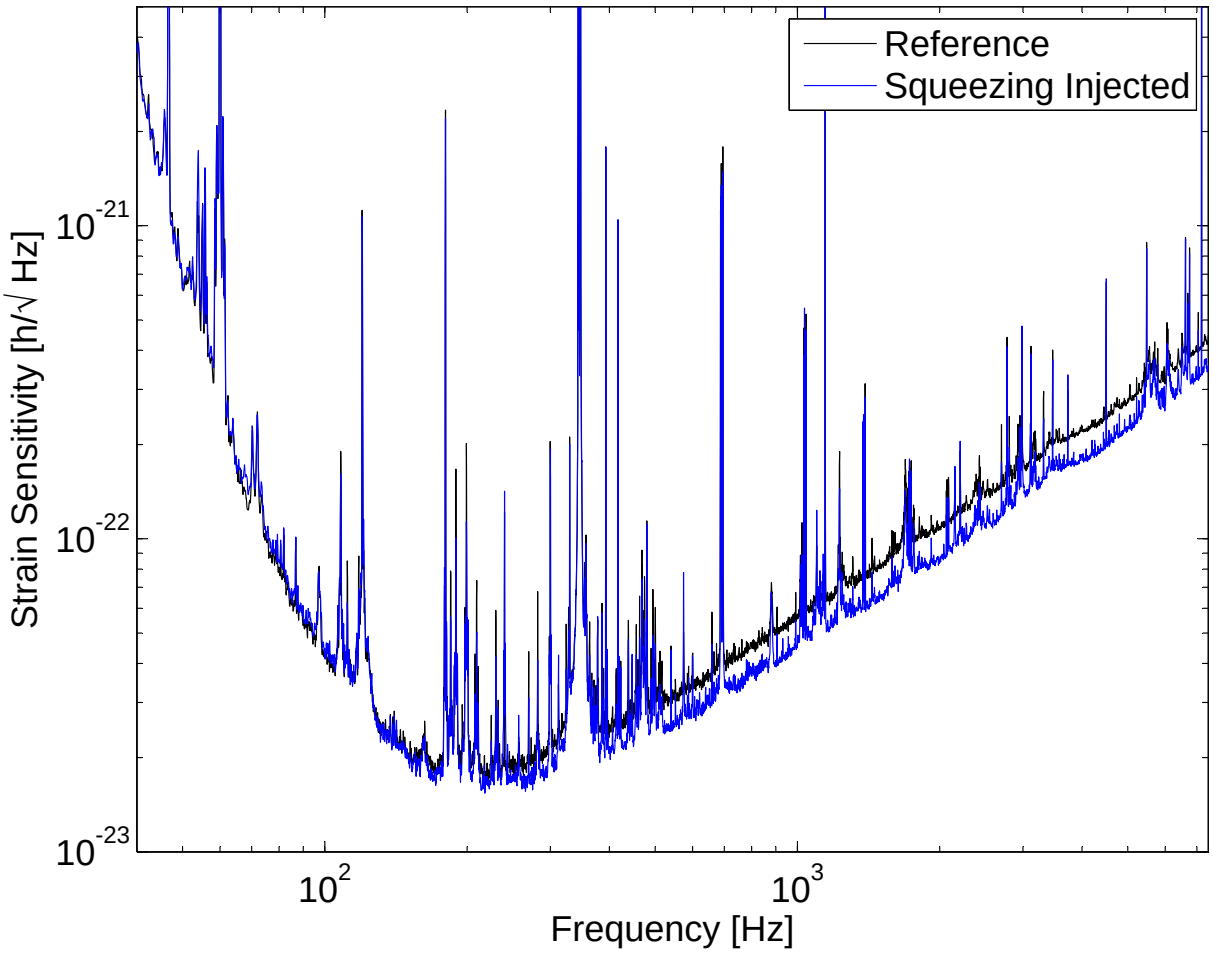

Figure 1-17: Enhanced LIGO sensitivity with squeezing injected. The reference trace shows the sensitivity of H1 without squeezing at the time of our experiment, with 20 Watts of input laser power. The blue trace shows the sensitivity with squeezing injected.

Importantly, there are no frequencies in this plot where the sensitivity with squeezing injected is worse than the reference, demonstrating for the first time that squeezing is compatible with the low frequency sensitivity of a full scale gravitational wave detector. Figure 1-18 shows the same data as 1-17, in the region around 200Hz where enhanced LIGO has the best sensitivity to gravitational waves. This is the first time that squeezing has been observed in a gravitational wave detector at those frequencies. This is the region where acoustically driven noise is expected to be largest, and we see no evidence of added acoustic noise with squeezing. Figure 1-19 shows the same data as 1-17 compared to the best sensitivity measured during the

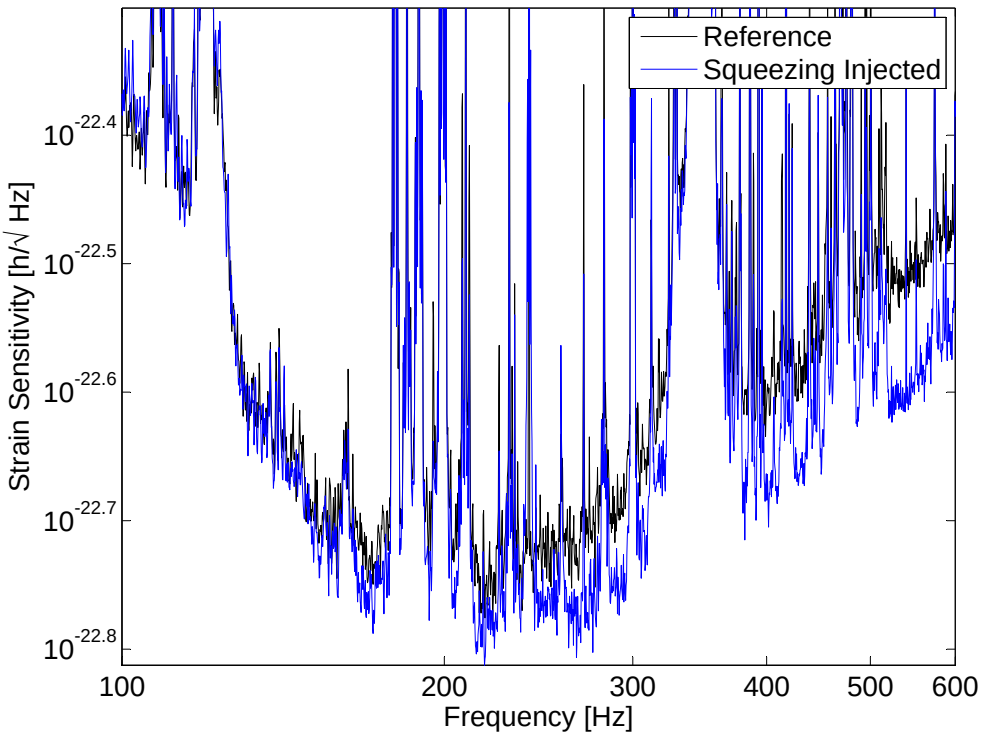

Figure 1-18: Squeezing enhancement in LIGO's most sensitive frequency band

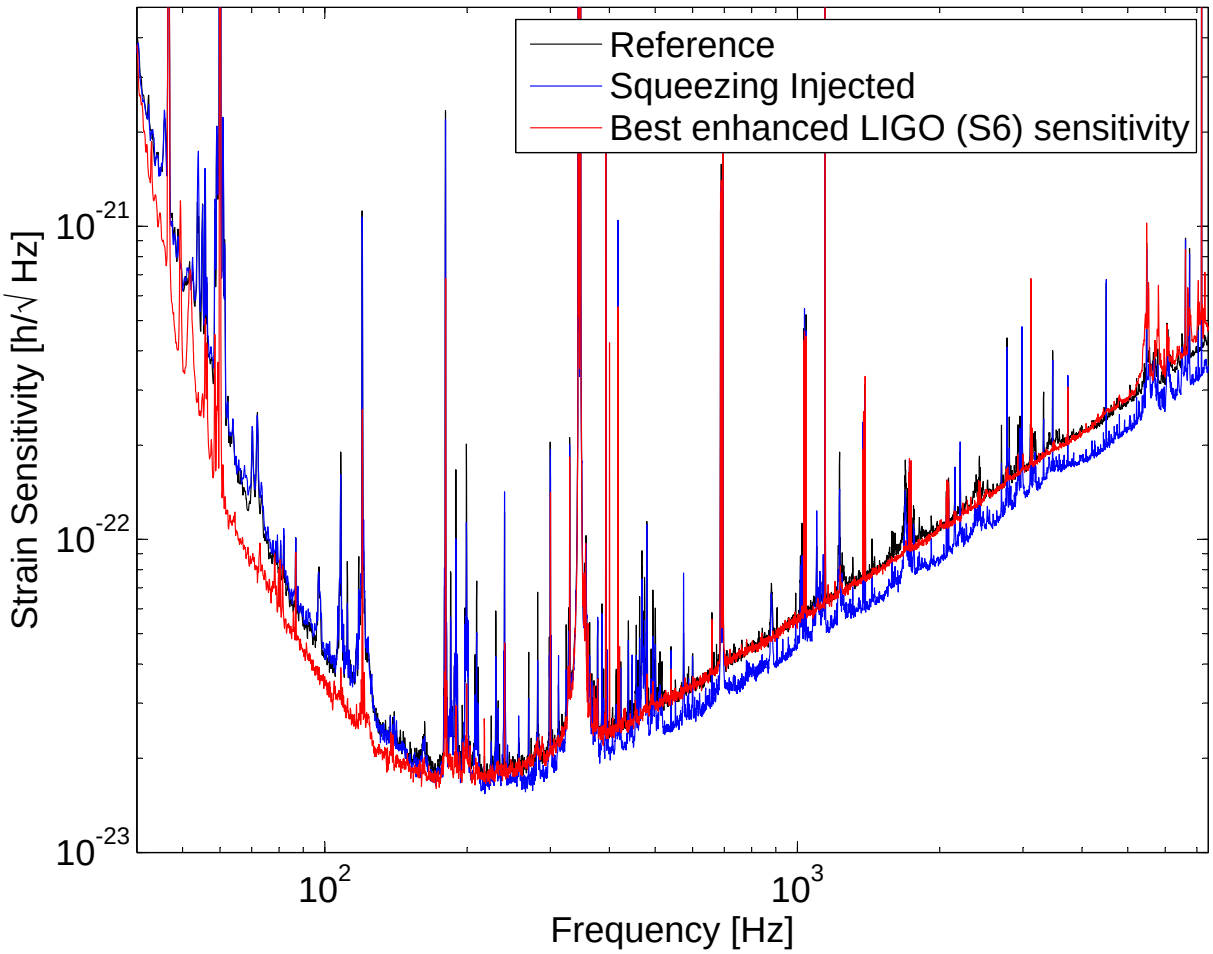

Figure 1-19: Squeezing results compared to enhanced LIGO's best sensitivity.

enhanced LIGO science run. The squeezing result represents the best broadband sensitivity in a gravitational wave detector to date. The best enhanced LIGO sensitivity was measured when the oceanic microseism, seismic motion from 0.1 to 0.4 Hz, was unusually low due to calm summer weather. This low frequency motion is unconverted into the lower end of LIGO sensitive band, limiting the sensitivity. During and the late November and early December squeezing experimental run, the microseism was unusually high, mostly above the 90th percentile. This explains the difference in the low frequency sensitivity, which is unrelated to squeezing.

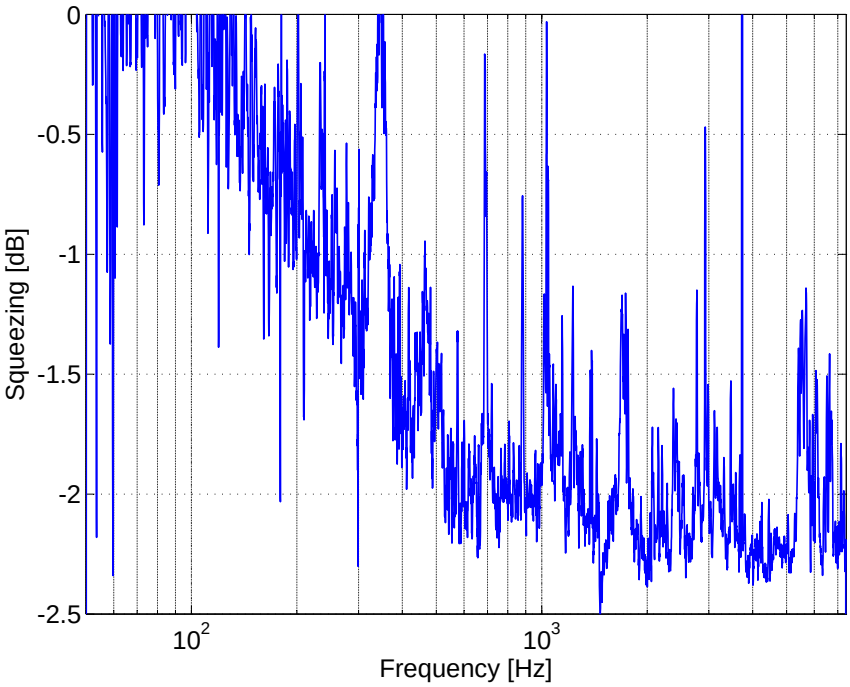

(a) More than 2dB of squeezing observed with 16 W r input power.

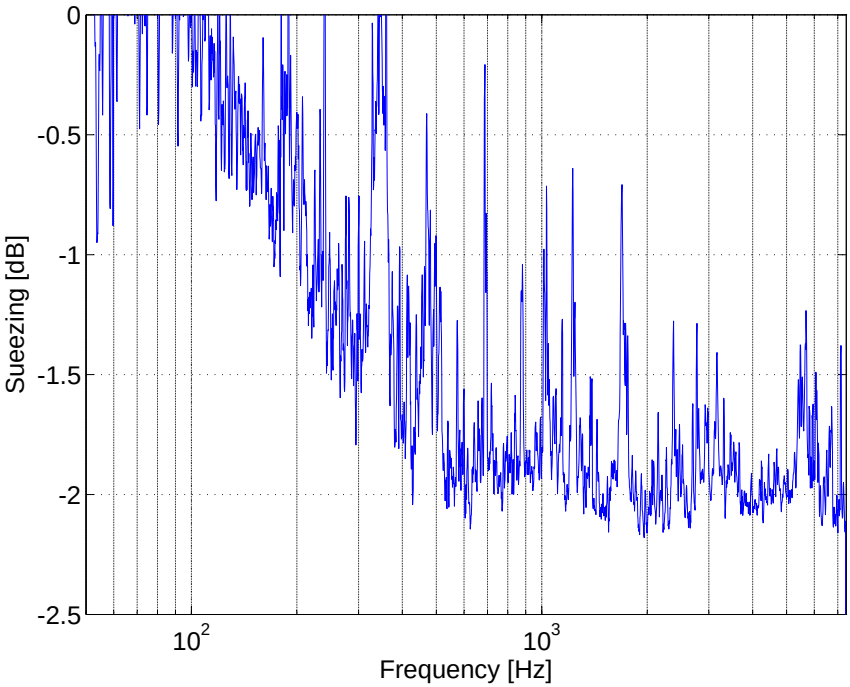

(b) Squeezing observed down to 100 Hz with 8 W input power.

Figure 1-20: Noise reduction due to squeezing, ratios of interferometer sensitivity with squeezing to sensitivity without squeezing, plotted on a log scale.

1.3.2 Astrophysical impact of squeezing enhancement

Plots in the previous section show the improvement in strain sensitivity due to squeezing, but the true benefit of squeezing will come from improvements in the sensitivity of the detector to realistic sources of gravitational waves. These results demonstrate for the first time that squeezing can improve the astrophysical reach of a gravitational wave detector when realistic assumptions about potential sources are used.

A commonly used metric for comparing the sensitivity of gravitational wave detectors is the horizon or sight distance for neutron star inspirals. This is the distance to which gravitational radiation from a binary of 1.4 $M_{\odot}$ neutron stars can be detected with a signal to noise ratio of 8, averaged over sky position and binary orientation. The low frequency sensitivity of a detector is most important for detection of inspirals, which emit at lower frequencies for longer times. The horizon distance for an inspiral is proportional to [44]:

$$d_{hor} = \Theta \left[\int df \frac{f^{-7/3}}{S_n(f)} \right]^{1/2} \tag{1.57}$$

where Θ is a constant that depends on the mass of the compact objects, and averaging over the sky positions and binary orientations. The power spectral density $S_n(f)$ is the square of the amplitude spectral densities plotted for example in 1-17. The improvement in inspiral range due to squeezing in the data from Figure 1-20a is shown in Figure 1-21. The nearly 1 Mpc improvement shown is due entirely to squeezing below 1kHz and represents a 7% increase in the detector's insprial range, most of the improvement is due to squeezing below 300Hz.

Nearby rapidly spinning neutron stars with deformations in the crust are another promising source for earth based gravitational wave detectors. In the intermediate frequencies from 300-600Hz, there are 28 known pulsars within 6 kpc [28]. The neutron star equation of state is not well understood, but observations of gravitational radiation from one of these known pulsars would provide new information about the neutron star's asymmetry, possibility caused by strong internal magnetic fields or asymmetries of the crust, and provide

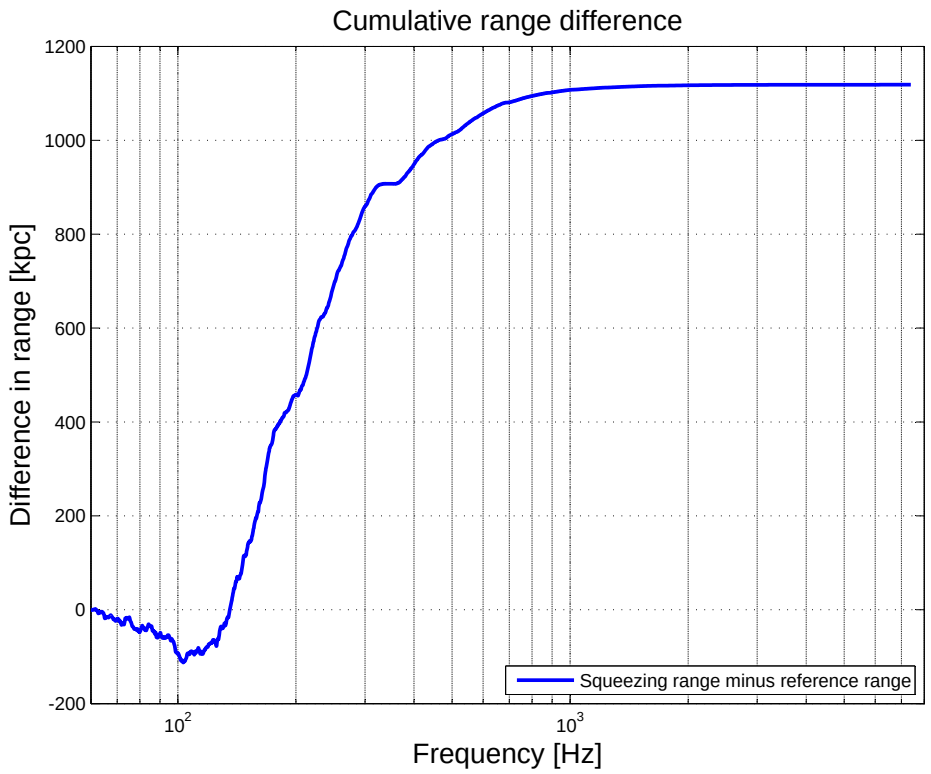

Figure 1-21: Improvement in insprial range due to squeezing, when interferometer input power was 16 Watts. This plot shows the difference in the cumulative insprial range with and without squeezing, and was calculated based on a script written by Grant Meadors [49]. Most of the nearly 1 Mpc improvement in range came from squeezing below 500 Hz, where the amount of squeezing was small. The small decrease in range at low frequencies was most likely due to changes in the seismic or environment in the short time between the time of the reference trace and the squeezing trace.

insight into this exotic state of matter [28]. At these frequencies the squeezing we observed would provide a 19% improvement in the SNR of any gravitational waves detected from these pulsars, and reduce upper limits from null detection by 16% [20]. Assuming that neutron stars in this frequency range are isotropically distributed within our galaxy this represents a factor of two increase in the number of detectable neutron stars for a detector with the level of squeezing we observed.

At the highest frequencies in LIGO's detection band, coalescences and mergers of compact binary systems are a primary astrophysics target. As neutron star binaries loose energy by

emitting gravitational waves the frequency of their orbits increase as the radius decreases, until the system reaches the radius of the innermost stable circular orbit, the ISCO. For a binary system of 1.4 $M_\odot$ neutron stars the orbital frequency at ISCO would be 800Hz, so the frequency of gravitational radiation would be 1.5kHz [26]. This means that the 26% increase in the signal to noise ratio due to squeezing at frequencies above 600 Hz can improve observations of this interesting stage of binary evolution.

Coalescing compact binaries are expected to have electromagnetic counterparts. An observation of a single event in both electromagnetic and gravitational radiation could offer more insight than either observation alone would, and increase confidence in an early gravitational wave detection. A real difficulty in triggering searches for electromagnetic counterparts based on a potential observation of gravitational waves is the large area of the sky that must be searched. The sky location of a gravitational wave source is estimated based on the difference in arrival times at different detectors. The timing error for binary coalescence is inversely proportional to the signal to noise ratio, and the solid angle on the sky that needs to be searched for counterparts to a signal detected in a network of two detectors is proportional to the timing error (assuming the detectors have the same timing accuracy) [26]. This means that the 2dB noise reduction we saw from squeezing would reduce the area of the sky to be searched by 20%.

We have demonstrated for the first time that squeezing is compatible with operation of a full scale gravitational wave interferometer with good low frequency sensitivity, and shown an improvement in the sensitivity to realistic sources of gravitational waves. These modest improvements would provide a benefit to the astrophysical output of a gravitational wave detector. However, the real significance of these results are that they have demonstrated the potential of squeezing in a full scale interferometer. The lessons learned from this experiment allow us to form a detailed plan for achieving a more significant noise reduction in the next generation of interferometric gravitational wave detectors.

Appendix A

Terminology

Optical parametric amplifier/ optical parametric oscillator: Some texts use OPO to refer to above threshold operation, and OPA when the crystal is single passed and not in a cavity or when the cavity is below threshold [6,35, p486]. Others call these above and below threshold operation. Sometimes OPA is used to refer to operation of a parametric down-converter in a cavity, below threshold when a seed beam is injected /citeMcKenzieThesis. In nonlinear optics text an OPO is doubly resonant if it is resonant for both the signal and idler fields [6]. OPO's used for single mode squeezing are degenerate, meaning that the signal and idler fields are at the same wavelength, so they are all doubly resonant in that sense. The term doubly resonant has also been used to refer to a degenerate OPO which is also resonant for the pump field.

Degenerate OPO- An OPO in which the signal and idler frequencies are the same. (as in OPO's used for quadrature squeezing, where the signal and ilder frequencies are at audio sidebands)

Doubly resonant OPO- In nonlinear optics literature this normally refers to an OPO which is resonant for both the signal and ilder fields [6]. It has also sometimes been used to refer to a degenerate OPO which is resonant for the fundamental and harmonic fields [69].

A.1 Acronyms

EOM	electro optic modulator
CLF	coherent locking field
OMC	output mode cleaner
LO-	local oscillator
OPA	optical parametric amplifier
OPO	optical parametric oscillator
PDH	Pound Drever Hall
PPTKTP	
PSL	Prestabilized laser
PZT	piezo electrivc transducer
SHG	second harmonic generator

Type I phase matching- Low frequency waves have the same polarization Type II phase matching- polarization of two lower frequency waves are orthogonal [6, p 81]

Appendix B

Procedure for optimizing crystal position

Bibliography

[1] Rich Abbott, Rana Adhikari, Stefan Balmer, Lisa Barsotti, Matt Evans, Peter Fritschel, Valera Frolov, Guido Mueller, Bram Slagmolen, and Sam Waldman. AdvLIGO Interferometer Sensing and Control Conceptual Design. Technical Report LIGO-T070247-010-I, LIGO DCC, 2008. Available at dcc.ligo.org.

[2] T. Aoki, G. Takahashi, and A. Furasawa. Squeezing at 946nm with periodically poled ktiopo4. *Optics Express*, 14(15):6930–6935, 2006.

[3] Lisa Barsotti. aLIGO Faraday: t=96%, Isolation 40 dB, but only 23 dB backscatter isolation. LHO ilog found at http://ilog.ligo-wa.caltech.edu/ilog/pub/ilog.cgi, For readonly access use username: reader Password: readonly, June 9th 2011.

[4] Lisa Barsotti. IFO light back to the squeezer (Expected). August 30th 2011.

[5] Lisa Barsotti. Sideband/carrier power @ 8W. LHO ilog found at http://ilog.ligo-wa.caltech.edu/ilog/pub/ilog.cgi, For readonly access use username: reader Password: readonly, November 29th 2011.

[6] Robert W. Boyd. *Nonlinear Optics*. Elsevier, Academic Press, Burlington, MA, 2008.

[7] Benjamin Buchler. *Electro-Optic Control of Quantum Measurements*. PhD thesis, Australian National University, September 2001.

[8] Carlton M. Caves. Quantum-mechanical noise in an interferometer. *Phys. Rev. D*, 23:1693–1708, Apr 1981.

[9] Carlton M. Caves and Bonny L. Schumaker. New formalism for two-photon quantum optics. i. quadrature phases and squeezed states. *Phys. Rev. A*, 31:3068–3092, May 1985.

[10] Simon Chelkowski. *Squeezed Light and Laser Interferometeric Gravitational Wave Detectors*. PhD thesis, Gottfried Wilhelm Leibniz Universitat Hannover, September 2007.

[11] Simon Chelkowski, Henning Vahlbruch, Karsten Danzmann, and Roman Schnabel. Coherent control of broadband vacuum squeezing. *Phys. Rev. A*, 75:043814, Apr 2007.

[12] S Chua, M Stefszky, C Mow-Lowry, B Buchler, S Dwyer, D Shaddock, P K Lam, and D McClelland. Backscatter tolerant squeezed light source for advanced gravitational-wave detectors. *Optics Letters*, 36(23):4680–4682, 2011.

[13] Sheon Chua. H1 Squeezing vs CLF input power. LHO ilog, October 10th 2011.

[14] Sheon Chua. Power returning back from HAM4 +polarization. LHO ilog, December 3rd 2011.

[15] LIGO Scientific Collaboration. A gravitational wave observatory operating beyond the quantum shot-noise limit. *Nature Physics*, volume(number):pages, September 2011.

[16] M. J. Collett and C. W. Gardiner. Squeezing of intracavity and traveling-wave light fields produced in parametric amplification. *Phys. Rev. A*, 30:1386–1391, Sep 1984.

[17] Katherine Dooley. *Design and performance of high laser power interferometers for gravitational-wave detection*. PhD thesis, Louisiana State University, 2011.

[18] P D Drummond and Z Ficek, editors. *Quantum Squeezing*. Atomic Optical and Plasma Physics. Springer-Verlag, Berlin, 2004.

[19] P.D. Drummond, K.J. McNeil, and D.F. Walls. Non-equilibrium transitions in sub/second harmonic generation. *Optica Acta: International Journal of Optics*, 27(3):321–335, 1980.

[20] Réjean J. Dupuis and Graham Woan. Bayesian estimation of pulsar parameters from gravitational wave data. *Phys. Rev. D*, 72:102002, Nov 2005.

[21] Sheila Dwyer. CLF noise gone. LHO ilog, November 21st 2011.

[22] Sheila Dwyer. Noise in darm proportional to CLF power. LHO ilog, October 24th 2011.

[23] Sheila Dwyer. Summary of Loss Measurements for H1 Squeezing Test. Technical Report LIGO-T1200023-v1, LIGO DCC, January 2012.

[24] Tobias Eberle, Sebastian Steinlechner, Jöran Bauchrowitz, Vitus Händchen, Henning Vahlbruch, Moritz Mehmet, Helge Müller-Ebhardt, and Roman Schnabel. Quantum enhancement of the zero-area sagnac interferometer topology for gravitational wave detection. *Phys. Rev. Lett.*, 104:251102, Jun 2010.

[25] Shai Emanueli and Ady Arie. Temperature-dependent dispersion equations for ktiopo4 and ktioaso4. *Appl. Opt.*, 42(33):6661–6665, Nov 2003.

[26] Stephen Fairhurst. Triangulation of gravitational wave sources with a network of detectors. *New Journal of Physics*, 11(12):123006, 2009.

[27] M.M. Fejer, G.A. Magel, D.H. Jundt, and R.L. Byer. Quasi-phase-matched second harmonic generation: tuning and tolerances. *Quantum Electronics, IEEE Journal of*, 28(11):2631 –2654, nov 1992.

[28] B. P. Abbott for the LIGO Scientific Collaboration. Searches for gravitational waves from known pulsars with science run 5 ligo data. *The Astrophysical Journal*, 713(1):671, 2010.

[29] Alexander Franzen, Boris Hage, James DiGuglielmo, Jaromir Fiurasek, and Roman Schnabel. Experimental demonstration of continuous variable purification of squeezed states. *Phys. Rev. Lett.*, 97:150505, Oct 2006.

[30] Tobin Fricke. *Homodyne Detection for Laser Interferometric Gravitational Wave Detectors*. PhD thesis, Louisiana State University, 2011. http://etd.lsu.edu/docs/available/etd-11082011-115541/unrestricted/frickediss.pdf.

[31] TObin Fricke. L1, H1 S6 shot noise estimates. LLO ilog, April 13th 2011.

[32] Tobin T Fricke, Nicols D Smith-Lefebvre, Richard Abbott, Rana Adhikari, Katherine L Dooley, Matthew Evans, Peter Fritschel, Valery V Frolov, Keita Kawabe, Jeffrey S Kissel, Bram J J Slagmolen, and Sam J Waldman. Dc readout experiment in enhanced ligo. *Classical and Quantum Gravity*, 29(6):065005, 2012.

[33] Peter Fritschel. Backscattering from the AS port:Enhanced and Advanced LIGO. Technical Report T060303-00, LIGO DCC, 2006.

[34] C. W. Gardiner and M. J. Collett. Input and output in damped quantum systems: Quantum stochastic differential equations and the master equation. *Phys. Rev. A*, 31:3761–3774, Jun 1985.

[35] J. C. Garrison and R. Y. Chiao. *Quantum Optics*. Oxford University Press, Oxford, 2008.

[36] Christopher C. Gerry and Peter L. Knight. *Introductory Quantum Optics*. Cambridge University Press, Cambridge, 2005.

[37] K. Goda, O. Miyakawa, E. E. Mikhailov, S. Saraf, R. Adhikari, K. McKenzie, R. Ward, S. Vass, A. J. Weinstein, and N. Mavalvala. A gravitational wave observatory operating beyond the quantum shot-noise limit. *Nature Physics*, 2008.

[38] Keisuke Goda. *Development of Techniques for Quantum Enhanced Laser-Interferometric Gravitational-Wave Detectors*. PhD thesis, Massachusetts Institute of Technology, 2007.

[39] Keisuke Goda, Kirk McKenzie, Eugeniy E. Mikhailov, Ping Koy Lam, David E. McClelland, and Nergis Mavalvala. Photothermal fluctuations as a fundamental limit to low-frequency squeezing in a degenerate optical parametric oscillator. *Phys. Rev. A*, 72:043819, Oct 2005.

[40] I. Juwiler, A. Arie, A. Skliar, and G. Rosenman. Efficient quasi-phase-matched frequency doubling with phase compensation by a wedged crystal in a standing-wave external cavity. *Opt. Lett.*, 24(17):1236–1238, Sep 1999.

[41] Kiyoshi Kato and Eiko Takaoka. Sellmeier and thermo-optic dispersion formulas for ktp. *Appl. Opt.*, 41(24):5040–5044, Aug 2002.

[42] Keita Kawabe, Luca Matone, and Joseph Betzwieser. Excess noise mechanism in ligo output mode cleaner. Technical Report LIGO-T040158-00-D, LIGO DCC, 2004.

[43] Alexander Khalaidovski, Henning Vahlbruch, Nico Lastzka, Christian Grf, Karsten Danzmann, Hartmut Grote, and Roman Schnabel. Long-term stable squeezed vacuum state of light for gravitational wave detectors. *Classical and Quantum Gravity*, 29(7):075001, 2012.

[44] Michele Maggiore. *Gravitational Waves Volume 1:Theory and Experiment*. Oxford University Press, Oxford, UK, 2008.

[45] Genta Masada, Tsuyoshi Suzudo, Yasuhiro Satoh, Hideki Ishizuki, Takunori Taira, and Akira Furusawa. Efficient generation of highly squeezed light with periodically poled mgo:linbo3. *Opt. Express*, 18(12):13114–13121, Jun 2010.

[46] Kirk McKenzie. *Squeezing in the Audio Gravitational Wave Detection Band*. PhD thesis, Australian National University, February 2008.

[47] Kirk McKenzie, Nicolai Grosse, Warwick P. Bowen, Stanley E. Whitcomb, Malcolm B. Gray, David E. McClelland, and Ping Koy Lam. Squeezing in the audio gravitational-wave detection band. *Phys. Rev. Lett.*, 93:161105, Oct 2004.

[48] Kirk McKenzie, Daniel A. Shaddock, David E. McClelland, Ben C. Buchler, and Ping Koy Lam. Experimental demonstration of a squeezing-enhanced power-recycled michelson interferometer for gravitational wave detection. *Phys. Rev. Lett.*, 88:231102, May 2002.

[49] Grant Meadors. Plots/graphs/figures of range and range integrand. LHO ilog, November 23rd 2011.

[50] Moritz Mehmet, Sebastian Steinlechner, Tobias Eberle, Henning Vahlbruch, André Thüring, Karsten Danzmann, and Roman Schnabel. Observation of cw squeezed light at 1550 nm. *Opt. Lett.*, 34(7):1060–1062, Apr 2009.

[51] Moritz Mehmet, Henning Vahlbruch, Nico Lastzka, Karsten Danzmann, and Roman Schnabel. Observation of squeezed states with strong photon-number oscillations. *Phys. Rev. A*, 81:013814, Jan 2010.

[52] Miguel Orszag. *Quantum Optics: Including Noise Reduction, Trapped Ions, Quantum Trajectories, and Decoherence*. Springer, Berlin Heidelberg New York, 2008.

[53] David J Ottaway, Peter Fritschel, and Samuel J. Waldman. Impact of upconverted scattered light on advanced interferometric gravitational wave detectors. *Optics Express*, 20(8):8329–8336, 2012.

[54] E. S. Polzik, J. Carri, and H. J. Kimble. Atomic spectroscopy with squeezed light for sensitivity beyond the vacuum-state limit. *Applied Physics B: Lasers and Optics*, 55:279–290, 1992. 10.1007/BF00325016.

[55] E. S. Polzik and H. J. Kimble. Frequency doubling with KNbO3 in an external cavity. *Opt. Lett.*, 16(18):1400–1402, Sep 1991.

[56] F J Raab and S E Whitcomb. Estimation of special optical properties of a triangular ring cavity. Technical Report T920004-00, LIGO DCC, February 1992.

[57] M Rakhmanov, R L Savage Jr, D H Reitze, and D B Tanner. Dynamic resonance of light in fabry-perot cavities. *Physics Letters A*, 305:239–44.

[58] Malik Rakhmanov. *Dynamics of Laser Interferometric Gravitational Wave Detectors*. PhD thesis, California Institute of Technology, May 2000.

[59] Robert Schofield. The impact of squeezing on vibration coupling to H1. LHO ilog, October 23rd 2011.

[60] Robert Schofield. Status of acoustic isolation of the H2 PSL enclosure. LHO alog available at alog.ligo-wa.caltech.edu/aLOG, September 19 2011.

[61] Bonny L. Schumaker and Carlton M. Caves. New formalism for two-photon quantum optics. ii. mathematical foundation and compact notation. *Phys. Rev. A*, 31:3093–3111, May 1985.

[62] Marlan O. Scully and M. Suhail Zubairy. *Quantum Optics*. Cambridge University Press, Cambridge, UK, 1997.

[63] Anthony E Siegman. *Lasers*. University Science Books, Mill Valley, CA, 1986.

[64] A. Sizmann, R.J. Horowicz, G. Wagner, and G. Leuchs. Observation of amplitude squeezing of the up-converted mode in second harmonic generation. *Optics Communications*, 80(2):138 – 142, 1990.

[65] Nicolas Smith-Lefebvre. *Techniques for Improving the Readout Sensitivity of Gravitational Wave Antennae*. PhD thesis, Massachusetts Institute of Technology, June 2012.

[66] Daniel A. Steck. Quantum and Atom Optics. available online at http://steck.us/teaching, (revision 0.8.3) 25 May 2012.

[67] M S Stefszky, C M Mow-Lowry, S S Y Chua, D A Shaddock, B C Buchler, H Vahlbruch, A Khalaidovski, R Schnabel, P K Lam, and D E McClelland. Balanced homodyne detection of optical quantum states at audio-band frequencies and below. *Classical and Quantum Gravity*, 29(14):145015, 2012.

[68] Michael Stefszky. New SHG characterization. LASTI ilog available at http://www.ligo.mit.edu/ilog/pub/ilog.cgi, July 9 2010.

[69] Michael Stefszky, Conor M Mow-Lowry, Kirk McKenzie, Sheon Chua, Ben C Buchler, Thomas Symul, David E McClelland, and Ping Koy Lam. An investigation of doubly-resonant optical parametric oscillators and nonlinear crystals for squeezing. *Journal of Physics B: Atomic, Molecular and Optical Physics*, 44(1):015502, 2011.

[70] John C Stover, editor. *Optical Scattering: Measurement and Analysis*. SPIE Optical Engineering Press, Bellingham Washington, 1995.

[71] Yuishi Takeno, Mitsuyoshi Yukawa, Hidehiro Yonezawa, and Akira Furusawa. Observation of -9 db quadrature squeezing with improvement of phasestability in homodyne measurement. *Opt. Express*, 15(7):4321–4327, Apr 2007.

[72] Henning Vahlbruch. *Squeezed Light for Gravitational Wave Astronomy*. PhD thesis, Gottfried Wilhelm Leibniz Universitt Hannover, 2008.

[73] Henning Vahlbruch, Simon Chelkowski, Boris Hage, Alexander Franzen, Karsten Danzmann, and Roman Schnabel. Demonstration of a squeezed-light-enhanced power- and signal-recycled michelson interferometer. *Phys. Rev. Lett.*, 95:211102, Nov 2005.

[74] Henning Vahlbruch, Alexander Khalaidovski, Nico Lastzka, Christian Grf, Karsten Danzmann, and Roman Schnabel. The geo600 squeezed light source. *Classical and Quantum Gravity*, 27(8):084027, 2010.

[75] D F Walls and Gerard J Milburn. *Quantum Optics*. Springer, Berlin, 2008.

[76] Min Xiao, Ling-An Wu, and H. J. Kimble. Precision measurement beyond the shot-noise limit. *Phys. Rev. Lett.*, 59:278–281, Jul 1987.

[77] Horace P. Yuen. Two-photon coherent states of the radiation field. *Phys. Rev. A*, 13:2226–2243, Jun 1976.